

Universidade de São Paulo
Instituto de Física

Antiferromagnetismo nos Titanatos
Geometricamente Frustrados
 $\text{Sm}_2\text{Ti}_2\text{O}_7$ e $\text{Nd}_2\text{Ti}_2\text{O}_7$

Lina Ishida

Orientador: Prof. Dr. Rafael Sá de Freitas

Dissertação de mestrado apresentada ao
Instituto de Física para a obtenção do
título de Mestre em Ciências

Banca Examinadora:

Prof. Dr. Rafael Sá de Freitas (IF-USP)
Prof. Dr. Artur Wilson Carbonari (IPEN)
Prof. Dr. Gabriel Adolfo Cabrera Pasca (UFPA)

São Paulo
2018

FICHA CATALOGRÁFICA
Preparada pelo Serviço de Biblioteca e Informação
do Instituto de Física da Universidade de São Paulo

Ishida, Lina

Antiferromagnetismo nos titanatos geometricamente frustrados
Sm₂Ti₂O₇ e Nd₂Ti₂O₇ / Antiferromagnetism in the geometrically
frustrated titanates Sm₂Ti₂O₇ and Nd₂Ti₂O₇. São Paulo, 2019.

Dissertação (Mestrado) – Universidade de São Paulo, Instituto de Física. Depto.
Física dos Materiais e Mecânica.

Orientador: Prof. Dr. Rafael Sá de Freitas

Área de Concentração: Física da Matéria Condensada

Unitermos: 1. Frustração magnética; 2. Pirocloro; 3. Magnetismo; 4. Materiais
magnéticos.

USP/IF/SBI-007/2019

University of São Paulo
Institute of Physics

Antiferromagnetism in the Geometrically
Frustrated Titanates
 $\text{Sm}_2\text{Ti}_2\text{O}_7$ and $\text{Nd}_2\text{Ti}_2\text{O}_7$

Lina Ishida

Supervisor: Prof. Dr. Rafael Sá de Freitas

Master dissertation submitted to the
Institute of Physics for the degree of
Master in Physics

Banca Examinadora:

Prof. Dr. Rafael Sá de Freitas (IF-USP)
Prof. Dr. Artur Wilson Carbonari (IPEN)
Prof. Dr. Gabriel Adolfo Cabrera Pasca (UFPA)

São Paulo
2018

for my friends.

“Wissenschaft und Kunst gehören der Welt an, und vor ihnen verschwinden die Schranken der Nationalität.” (Johann Wolfgang von Goethe)

Acknowledgements

"Some people go to priests; others to poetry; I to my friends, I to my own heart, I to seek among phrases and fragments something unbroken — I to whom there is not beauty enough in moon or tree; to whom the touch of one person with another is all, yet who cannot grasp even that, who am so imperfect, so weak, so unspeakably lonely. There I sat." (Virginia Woolf - "The Waves")

Agradeço primeiramente aos meus pais e ao meu irmão por possibilitarem a formação privilegiada que tive. Agradeço à minha mãe por me ensinar tudo o que sei hoje, especialmente a ser uma boa pessoa. Agradeço à Tama pelos 15 anos.

Agradeço às minhas amigas: Stephany, Mariane, Marina e Ana (em ordem cronológica) pois a vida seria impossível sem vocês. Obrigada por acreditarem no meu potencial e por não me deixarem desacreditar nele; obrigada por me motivarem a ser sempre melhor; obrigada por serem companheiras de vida e por provarem todos os dias que existem boas pessoas neste mundo; obrigada, por fim, por acrescentarem tanto à minha vida! Sté, obrigada por ser uma irmã por todos esses anos e por estar sempre ao meu lado! Agradeço também, com muito carinho, aos pais e irmãos da Stephany, Mariane e Marina por sempre me acolherem como uma filha/irmã em seus lares.

Agradeço aos amigos da Física: Gustavo e Fred, por serem as melhores pessoas com as quais eu poderia dividir um laboratório e por todo o carinho e apoio que me ofereceram em tantos momentos difíceis nestes últimos seis anos. Obrigada por fugirem ao estereótipo de estudantes de exatas e possuírem um coração tão gentil! Gustavo, obrigada por me salvar neste mestrado!

Agradeço aos professores da Letras que tornaram a minha decisão de mudar de carreira mais difícil; agradeço também aos professores do IF que tiveram o carinho e a dedicação de tirar minhas dúvidas constantemente.

Agradeço a todos do DFMT que me auxiliaram em algum momento deste trabalho, em especial ao Luciano, Sérgio, Paulo e Alan, por auxiliarem com equipamentos e com o trato das minhas amostras. Agradeço ao Antônio Carlos e Társis, da Física Aplicada, por auxiliarem diversas vezes com o manuseio dos equipamentos de Raio-X. Agradeço à dr^a Marina Leite e ao professor Flávio Vichi, do IQ, pelo preparo das amostras policristalinas estudadas neste trabalho. Agradeço ao Everton e ao Pablo por me ensinarem e auxiliarem durante os primeiros anos de IC.

Agradeço, com carinho, a todos os alunos do IQ que eu tive o prazer de conhecer nas monitorias (em especial, ao Victor e à Ana, novamente!) e com os quais aprendi muito mais do que imaginam.

Agradeço a todos do IFGW que me receberam de braços abertos e já me fazem sentir parte do grupo (em especial, ao grupo do professor Ricardo Urbano)!

Agradeço, com muito carinho, a todos os professores, alunos e funcionários do Atelier de La Musique que me inspiraram e me motivaram a superar muitas dificuldades.

Agradeço novamente e sempre aos meus amigos: Ana, Gustavo, Marianie, Stephany e Victor por colaborarem ativamente na elaboração da minha apresentação de defesa e possibilitarem a obtenção do meu título de mestre.

Agradeço a todos os compositores cujas obras me trouxeram a calma para continuar o meu trabalho e por despertarem minha paixão por música. Agradeço aos escritores que consolidaram a importância da arte na minha vida.

O presente trabalho foi realizado com apoio da Coordenação de Aperfeiçoamento de Pessoal de Nível Superior – Brasil (CAPES) – código de financiamento 001.

Resumo

Recentemente, observamos na comunidade científica o despertar de um interesse pelo estudo de titanatos de lantanídeo (terras-raras); neste íterim, as amostras $\text{Sm}_2\text{Ti}_2\text{O}_7$ e $\text{Nd}_2\text{Ti}_2\text{O}_7$ se destacam por terem sido pouco exploradas, especialmente a baixas temperaturas. Análises cristalográficas de monocristais de $\text{Sm}_2\text{Ti}_2\text{O}_7$ e $\text{Nd}_2\text{Ti}_2\text{O}_7$ nos permitiram confirmar inicialmente características de rede como a geometria cúbica e monoclínica, respectivamente, enquanto as análises magnéticas e calorimétricas forneceram a temperatura de transição, até então inédita no caso do $\text{Nd}_2\text{Ti}_2\text{O}_7$ (aproximadamente $T=0,62\text{K}$), além de ordenamento do tipo antiferromagnético e presença de anisotropia a altas temperaturas, na amostra de $\text{Sm}_2\text{Ti}_2\text{O}_7$, e por toda a extensão de temperaturas trabalhadas, na amostra de $\text{Nd}_2\text{Ti}_2\text{O}_7$. Por fim, identificamos também a entropia esperada para spins do tipo Ising em ambas as amostras.

Palavras-chave: Titanatos, Frustração Geométrica, Antiferromagnetismo, Pirocloro, Spin Ising.

Abstract

Recently the scientific community has shown interest for titanium lanthanides (rare-earth), with the titanates $\text{Sm}_2\text{Ti}_2\text{O}_7$ and $\text{Nd}_2\text{Ti}_2\text{O}_7$ being poorly approached, specially at low temperatures. Crystallographic analysis were performed on the single crystal samples of $\text{Sm}_2\text{Ti}_2\text{O}_7$ and $\text{Nd}_2\text{Ti}_2\text{O}_7$, which allowed us to confirm its expected cubic and monoclinic structures, respectively; Magnetic and calorimetric data displayed the transition temperature, not previously seen in case of $\text{Nd}_2\text{Ti}_2\text{O}_7$, of $T=0.35\text{K}$ and $T=0.62\text{K}$, respectively, and the antiferromagnetic behaviour of both samples; Anisotropy was observed at high temperatures on the $\text{Sm}_2\text{Ti}_2\text{O}_7$ data and along all the temperature range studied for the $\text{Nd}_2\text{Ti}_2\text{O}_7$ sample. Finally, we have identified the entropy of Ising spins on both samples.

Key-words: Titanates, Geometric Frustration, Antiferromagnetism, Pirochlore, Ising Spin.

Contents

Chapter 1 Introduction.....	11
Chapter 2 Magnetism, an Introduction.....	13
Chapter 3 Specific Heat.....	25
Chapter 4 An Introduction to Crystallography.....	33
Chapter 5 Recent Studies.....	40
Chapter 6 Experimental Procedure.....	43
Chapter 7 Results and Discussion: $\text{Sm}_2\text{Ti}_2\text{O}_7$	53
Chapter 8 Results and Discussion: $\text{Nd}_2\text{Ti}_2\text{O}_7$	63
Chapter 9 Conclusion.....	79
Chapter 10 References.....	81

List of Figures

Fig. 1: Spin arrangement of ion Mn^{2+} in manganese oxide MnO . We can observe the presence of two lattices of spin, pointing to opposite directions, in the diagonal direction. 17

Fig. 2: Behavior of magnetic susceptibility in function of temperature for magnetic phases Paramagnetism, Ferromagnetism and Antiferromagnetism. Below we see the description of Curie law and Curie-Weiss law, being C the Curie constant, T_c the critical temperature, T_N the Néel temperature (critical temperature for Antiferromagnets) and θ the Curie-Weiss temperature. Here, the “complex behavior” indicates the absence of a single model to describe the behavior below critical temperatures of ferromagnets. 17

Fig. 3: Geometrically frustrated system, where Ising spins can't find a single antiferromagnetic configuration of minimal energy in (a) 2D and (b) 3D configurations. 21

Fig. 4: Kagomé and Pyrochlore lattices, from left to right..... 21

Fig.5: configuration of hydrogen (black circles) and oxygen atoms (white circles) in ice, analogous to the “two in-two out” system of spins pointing inside and outside the tetrahedra configuration, as noticed by Pauling..... 22

Fig. 6: Behaviour of the inverse of susceptibility for an antiferromagnet. We can also notice where the characteristic temperatures θ and T_c occur. 23

Fig. 7: the pyrochlore lattice of corner-shared tetrahedra: here, we see the tetrahedra composed by the cations A (blue circles) only while cations B (green circles) are not connected as tetrahedra. The Oxygen atoms are represented by red circles. We can easily spot the presence of symmetry along the direction (111), the diagonal of the cube..... 23

Fig. 8: the perovskite lattice of octahedra. Here we can observe eight octahedra with oxygen in its corners with ion A trapped inside and ion B inside each octahedra..... 24

Fig.9: Spin wave configuration viewed from perspective and from above. This behavior occurs at presence of any thermal agitation in the system. 29

Fig. 10 : Lattice plane crossing the primitive vectors axes, being a_n axes and x_n points of intersection in the respective axis. 37

Fig. 11: Bragg formulation for reflection by two consecutive lattices separated by d 39

Fig.12: Geometrical condition for the occurrence of diffraction 39

Fig. 14: “all in-all out” configuration of $Sm_2Ti_2O_7$ 42

Fig. 15: $\text{Nd}_2\text{Ti}_2\text{O}_7$ atomic disposition, known as “layered perovskite”(LP), where octahedra composed by oxygen atoms in its vertices and a titanium atom in its center are asymmetrically disposed, in opposition to the highly symmetric structure of perovskite, with atoms of neodymium in its surroundings.	43
Fig. 16: single crystal of the sample $\text{Sm}_2\text{Ti}_2\text{O}_7$, with approx. 6cm of width and a diameter of 8-9mm, transparent to light with a deep red colour.	45
Fig. 17: X-Ray diffractometer θ - 2θ with Bragg-Brentano geometry.	46
Fig. 18: diffractometer theta-2theta, Bragg-Brentano geometry, at FAP (USP).	46
Fig. 19: Laue back-scattering schematization. Here, a film is put between the sample and the incident X-Ray; The X-Ray is diffracted and forms different patterns for each crystallographic group and direction.....	47
Fig.20: triple-axis goniometer used to find the crystal directions. The sample is placed in the indicated spot while the goniometer can be moved in the three indicated directions, with a high precision. Taken from the Crystal Growth Lab (DCMPMS, TIFR) page, from Mumbai, India.....	47
Fig.21 : 7 Tesla SQUID Magnetometer from Quantum Design (MSMS); 1.8 - 400K. AC & DC	48
Fig. 22: simplified scheme of the SQUID. L is the inductance, I the electrical current, V the voltage and M, the magnetization.....	49
Fig.23 : ZFC and FC curves for a sample of LaCuO_3	49
Fig. 24: VSM magnetometer with 20 T superconducting coil and He-3 Cryostat for measurements down to 0.5 T (left) followed by a simplified schematization of a VSM (right): (1) loud-speaker transducer, (2) conical paper cup support, (3) drinking straw, (4) reference sample, (5) sample, (6) reference coils, (7) sample coils, (8) magnet poles, (9) metal container.	50
Fig.25 : 3-ac-susceptometer with 7.5 T superconducting coil and diffusion pumped He-3 glass cryostat for measurements down to 0.35 K.....	51
Fig. 26: primary and secondary coils position inside the susceptometer.....	52
Fig. 27: Sample platform schematization of the PPMS.....	52
Fig. 28: diffraction pattern found for the directions (110) and (111), from left to right, with the help of software Clip.	55
Fig. 29: X-ray diffraction data from our sample of crushed crystal (blue) and the data found in ref [23] overlapped.....	56
Fig. 30: ZFC and FC curves for the crystal of $\text{Sm}_2\text{Ti}_2\text{O}_7$ along the orientations a) (111) and b) (110), at a applied field of 100 Oe.	57

Fig.31: Susceptibility of crystal (at (110) and (111) directions) and powder samples, with the susceptibility fitting used in Singh et al. (73) applied at the range of 4-20K, on the inset.....	58
Fig. 32: Magnetization in function of field, at temperature $T=2K$, in comparison with experimental data found in.....	58
Fig. 33: Specific Heat data of a single crystal sample of $Sm_2Ti_2O_7$ measured at zero field and oriented in a random direction. The curve is a guide to the eye.....	60
Fig. 34: Subtraction of lattice contribution at low temperatures, at $H=0T$, for a single crystal sample of $Sm_2Ti_2O_7$ oriented at a random direction; Specific Heat normalized by mol of Lanthanide (either Sm or Lu). In a) , we see the raw data of specific heat for both compounds $Sm_2Ti_2O_7$ and $Lu_2Ti_2O_7$ and in b) , the non-magnetic data after dividing it by an arbitrary factor of 1.9 to approximate it to the magnetic data of $Sm_2Ti_2O_7$	61
Fig. 35: a) Specific heat data under several values of applied field, for crushed crystal (polycrystalline) sample near transition range and b) phase diagram for both polycrystalline and single crystal (oriented in direction (111)) samples.	62
Fig. 36: Linear fitting in the heat capacity data for a single crystal sample of $Sm_2Ti_2O_7$ oriented at a random direction, in T^3 , at low temperatures ($T<0.34K$) and zero field, which corresponds to the magnon contribution of an Antiferromagnetic system.	63
Fig.37: Comparison between the data acquired in this work (dark pink) and the data from the reference papers (cyan), both single crystal samples.....	64
Fig.38: Variation of entropy for a single crystal sample of $Sm_2Ti_2O_7$ in comparison with the expected value of $R\ln 2$ expected for a Ising spin system. Results derived from the integration of magnetic specific heat data between the interval 0.05-6K.....	65
Fig.39: diffraction pattern found for the direction (100) of the single crystal sample of $Nd_2Ti_2O_7$; On the left, we see the theoretical dots for the direction (100) given by the software Clip and on the right, the image derived from the Laue backscattering.	67
Fig. 40: diffraction pattern for the direction (001) of the single crystal sample of $Nd_2Ti_2O_7$, given by the software Clip.....	67
Fig. 41: X-ray diffraction data from our sample of powder originated from sol-gel synthesis (pink) and the data found in ref for a single crystal sample of $Nd_2Ti_2O_7$	68
Fig. 42: Inverse of susceptibility for the polycrystalline and single crystal in directions (100), (010) and (001) for the $Nd_2Ti_2O_7$ sample.	69
Fig. 43: Magnetization in function of field for three crystallographic directions and powder sample, for $T=2K$	71
Fig. 44: Susceptibility in function of temperature. A pronounced transition peak is observed at $T=600mK$	72

Fig. 45: Heat capacity of single crystal and polycrystalline sample, with transition temperature at 0.62K, for zero field.....	73
Fig. 46: Schottky anomaly analysis applied to heat capacity data in function of temperature, for several values of field, for the polycrystalline sample.....	74
Fig. 47: a) Lattice subtraction following the dependence in T^3 b) Heat Capacity for a single crystal sample in direction (100) before and after lattice subtraction. The measurement was taken at $H=0T$	75
Fig. 48: a) Specific heat data under several values of applied field, for crushed crystal (polycrystalline) sample near transition range and b) phase diagram for single crystal (oriented in direction (100)).	76
Fig. 49: Specific heat at low fields (left) and higher fields (right).	77
Fig. 50: Linear fitting in the heat capacity data, in T^3 , at low temperatures ($T<0.34K$), which corresponds to the magnon contribution of an Antiferromagnetic system. The measurements were taken at $H=0T$	78
Fig.51: Variation of entropy of single crystal and polycrystalline samples of $Nd_2Ti_2O_7$ in comparison with the expected value of entropy for a Ising spin system. Results derived from the integration of magnetic specific heat data between the interval 0.19-10K.	79

List of Tables

Table 1: Bravais lattices according to lattice parameters of angle and axes
.....34

Table 2: parameters derived from the fitting proposed in [10] in comparison with the data presented at the same ref., for a crystal in direction (111), and our three types of sample.....56

Table 3: parameters derived from Curie-Weiss fitting of data in all three directions of single crystal and powder in comparison with the data found by Xing et al. for both directions (100) and (001) and powder samples in ref.....78

Chapter 1

Introduction

“Der Inhalt der Physik geht die Physiker an, die Auswirkungen alle Menschen”

(Friedrich Dürrenmatt – die Physiker)

Magnetic frustration has been recently investigated in many phenomena and rare-earth titanates in particular exhibit anomalous magnetic ordering at low temperatures such as spin ice ($\text{Dy}_2\text{Ti}_2\text{O}_7$ and $\text{Ho}_2\text{Ti}_2\text{O}_7$), spin liquid ($\text{Tb}_2\text{Ti}_2\text{O}_7$) and spin glass, which involves a series of complex phenomena based on a quantum overview. The samples of $\text{Sm}_2\text{Ti}_2\text{O}_7$ and $\text{Nd}_2\text{Ti}_2\text{O}_7$, in particular, have been poorly explored for its low magnetic moment and high asymmetry, respectively. Recently it has been discovered important applications for these materials such as photocatalysis and immobilization of nuclear waste. In this work, we are concerned about working with those samples not fully explored yet (specially at low temperatures in order of mK), which may add rich information to the research on the field of magnetic properties of materials.

In **Chapter 2**, we discuss some of the fundamental concepts of magnetism: types of magnetic ordering, interactions and theoretical models for each case. Since this work revolves around antiferromagnetic samples, we’ve centered our discussion around features that characterize this type of ordering.

In **Chapter 3**, we look above the theoretical basis of specific heat and the mathematical models for each mode of thermal energy: the magnetic, electronic and lattice contributions. Besides, we also discuss some interesting models we observe as the spin wave and Schottky effect.

In **Chapter 4**, we do a brief introduction to Solid State physics, only highlighting theoretical points that were necessary to work with the information in this work. That includes a bit of crystallography necessary to work with X-Ray diffraction and the Laue backscattering method; The principals of Magnetic Frustration, emphasizing the pyrochlore lattice and the rare-earth ions, which were our object of study.

In **Chapter 5**, we enlist some of the interesting and new information presented by the few papers that have worked with our samples in order to later compare them with our results. It includes data presented for the sample of $\text{Er}_2\text{Ti}_2\text{O}_7$, a pyrochlore structure that has called attention recently and may serve us for the similarity presented in the cubic structure as for the $\text{Sm}_2\text{Ti}_2\text{O}_7$.

In **Chapter 6**, we start to discuss our experimental procedure, talking a bit about the synthesis and preparation of the samples, the X-Ray diffraction and single crystal orientation and how the devices used for magnetic and calorimetric measurements work.

In **Chapter 7**, we already discuss the data for our first sample analysed: $\text{Sm}_2\text{Ti}_2\text{O}_7$. We make this discussion starting by the Laue backscattering diffraction method and go to the magnetic susceptibility, Curie-Weiss and specific heat analysis. We will discuss important features such as the possible presence of anisotropy at high temperatures and the antiferromagnetic behaviour.

In **Chapter 8**, we studied the samples of $\text{Nd}_2\text{Ti}_2\text{O}_7$, both single crystal and polycrystalline samples. We can see the high anisotropy of the sample and the antiferromagnetic ordering in both samples. We have also seen the transition peak that hasn't been reported yet.

In **Chapter 9**, we highlight some of the main results we derived in the past two chapters and discuss briefly the future of this work.

Chapter 2

Magnetism, an introduction

The way the magnetic moments inside a material react to the field will characterize a magnetic phase, which may be classified as diamagnetism, paramagnetism, ferromagnetism or antiferromagnetism. As we alter the temperature or even the pressure of the material, it can switch from one magnetic phase to another. [1]

In this first theoretical background chapter, we briefly discuss some of the most important concepts concerning magnetism, starting with basic concepts on magnetism, following through types of magnetic ordering and types of interactions, and finishing with an interesting phenomena that may occur on certain configurations, known as magnetic frustration.

2.1 Fundamental Concepts

When talking about magnetism, the first useful concept worth mentioning is the susceptibility, which analyses the relation between the variation of magnetization \mathbf{M} and the variation of applied external field \mathbf{H} :

$$\chi = \frac{\partial \mathbf{M}}{\partial \mathbf{H}} \quad (1)$$

Where \mathbf{M} can be given by the variation of Helmholtz free energy F :

$$\mathbf{M} = -\frac{N}{V} \frac{\partial F}{\partial \mathbf{H}} \quad (2)$$

Being $F \equiv U - TS$, where U is the internal energy of the system, T the temperature and S , the entropy. The behavior of the susceptibility is one most common way of determining the magnetic phase of the material.

Considering an uniform magnetic field \mathbf{H} along the z-axis, we can write the Hamiltonian for a single atom with its field dependence by:

$$\Delta\mathcal{H} = \mu_B(\mathbf{L} + g_0\mathbf{S}) \cdot \mathbf{H} + \frac{e^2}{8mc^2} H^2 \sum_i (x_i^2 + y_i^2) \quad (3)$$

Where \mathbf{L} is the orbital angular moment and \mathbf{S} is the total spin moment. Inserting the results of perturbation theory to the second order, we can write the Hamiltonian model which better suits the studies in magnetism as below:

$$\Delta\mathcal{H}_n = \mu_B \mathbf{H} \cdot \langle n | \mathbf{L} + g_0 \mathbf{S} | n \rangle + \sum_{n' \neq n} \frac{|\langle n | \mu_B \mathbf{H} \cdot (\mathbf{L} + g_0 \mathbf{S}) | n' \rangle|^2}{E_n - E_{n'}} + \frac{e^2}{8mc^2} H^2 \langle n | \sum_i (x_i^2 + y_i^2) | n \rangle \quad (4)$$

The simplest situation is for an ion with all electronic shells complete, in which case we will have:

$$\mathbf{J} | 0 \rangle = \mathbf{L} | 0 \rangle = \mathbf{S} | 0 \rangle = 0 \quad (5)$$

And the Hamiltonian will be simply:

$$\Delta\mathcal{H}_0 = \frac{e^2}{8mc^2} H^2 \langle 0 | \sum_i (x_i^2 + y_i^2) | 0 \rangle \quad (6)$$

Which represents a first-order shift in the ground state energy. In this system, the probability of the ion being found in a state different from the fundamental one is expressed in the susceptibility by:

$$\chi = -\frac{N}{V} \frac{\partial F}{\partial \mathbf{H}} = -\frac{N}{V} \frac{\partial^2 \Delta\mathcal{H}_0}{\partial H^2} = -\frac{e^2}{6mc^2} \frac{N}{V} \langle 0 | \sum_i (x_i^2 + y_i^2) | 0 \rangle \quad (7)$$

This is known as the Larmor diamagnetic susceptibility. Notice that we denominate diamagnetism the situation in which the applied magnetic field opposes the magnetic moment induced inside the material, resulting in a negative susceptibility. [9]

When we have a more generic situation where the ion has unfilled shells, we may distinguish two situations: When $\mathbf{J}=0$, where the Hamiltonian of the system will be written as:

$$\Delta\mathcal{H}_0 = \frac{e^2}{8mc^2} H^2 \langle 0 | \sum_i (x_i^2 + y_i^2) | 0 \rangle - \sum_n \frac{|\langle 0 | \mu_B \mathbf{H} \cdot (\mathbf{L} + g_0 \mathbf{S}) | n \rangle|^2}{E_n - E_0}$$

(8)

Where the second part of the equation will favor the alignment of the moment with the external field, which is known as Van Vleck Paramagnetism. Now, for the second situation when the sub level $J=0$ doesn't exist, when the separation between the fundamental state and the first excited state is much bigger than $k_B T$, being k_B the Boltzmann constant, only the states $2J+1$ will be relevant to the total energy and the term corresponding to the exchange energy on the Hamiltonian can be said to be proportional to the interaction between the field and a magnetic moment given by:

$$\mu = -g\mu_B J$$

(9)

Where g is the Landé factor. We can calculate the free energy for $2J+1$ states by the partition function:

$$e^{-\beta F} = \sum_{J_z=-J}^J e^{-\beta \gamma H J_z}$$

(10)

Where $\gamma = g\mu_B$ and $\beta = (k_B T)^{-1}$. The sum can be easily developed and the magnetization for N ions in a volume V will be given by:

$$\mathbf{M} = -\frac{N}{V} \frac{\partial F}{\partial H} = \frac{N}{V} \gamma J B_J \quad (11)$$

Where B_J is the Brillouin function given by:

$$B_J(x) = \frac{2J+1}{2J} \coth \frac{2J+1}{2J} x - \frac{1}{2J} \coth \frac{1}{2J} x \quad (12)$$

In the limit $\gamma H \ll k_B T$, we can expand the $\coth(x)$ function and derive the following expression for susceptibility:

$$\chi = \frac{N}{V} \frac{(g\mu_B)^2 J(J+1)}{3 k_B T}$$

$$= \frac{N}{V} \frac{1}{3} \frac{\mu_B^2 p^2}{k_B T} \quad (13)$$

where p is defined as:

$$p = \frac{\mu_{eff}}{\mu_B} = g[J(J + 1)]^{1/2} \quad (14)$$

This inverse dependence of susceptibility with temperature is called Curie law.

2.2 Magnetic Ordering

Most of solids doesn't display spontaneous magnetic ordering, presenting a weak internal field when in presence of an applied external field. These systems are called Paramagnetism. It is important to remark that all materials present Paramagnetism until the critical temperature, below which the magnetic ordering occurs. [9]

Ferromagnetism is the most common phase in which we observe a spontaneous ordering of magnetic moment. It means that the configuration of the material is such that the ordering of moment occurs even in the absence of an external field. This can be due to the existence of exchange interactions and the ordering is destroyed above critical temperature.

When the sum of the individual moments is zero, we classify it as an antiferromagnetic system. We can think of it as two sublattices of parallel spins, each one pointing in opposite directions, and obeying the general model for ferromagnetism. Since the antiferromagnetic system doesn't show any macroscopic field, a good way to work out the situation is using Neutron diffraction. This technique allows us to investigate locally the presence of magnetic moment since the magnetic scattering can be distinguished from the non-magnetic ones because the last ones doesn't last while changing temperature and external field. Notice also that neutrons carry magnetic moment and this magnetic moment interact with the magnetic moment from the sample studied. We can see as an example the configuration of ion Mn^{2+} , in the fig. 1, where we see how the spins in plane (111) are parallel but in any plane adjacent to that are antiparallel. [1]

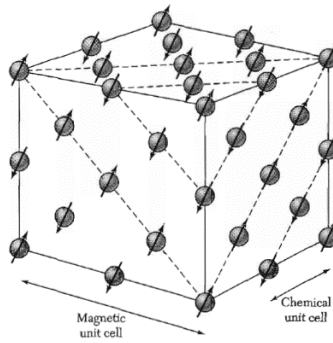


Fig.1: Spin arrangement of ion Mn^{2+} in manganese oxide MnO . We can observe the presence of two lattices of spin, pointing to opposite directions, in the diagonal direction. [1]

The susceptibility in an antiferromagnetic system doesn't grows indefinitely at low temperatures but presents a cusp, as we see in the fig.2 below.

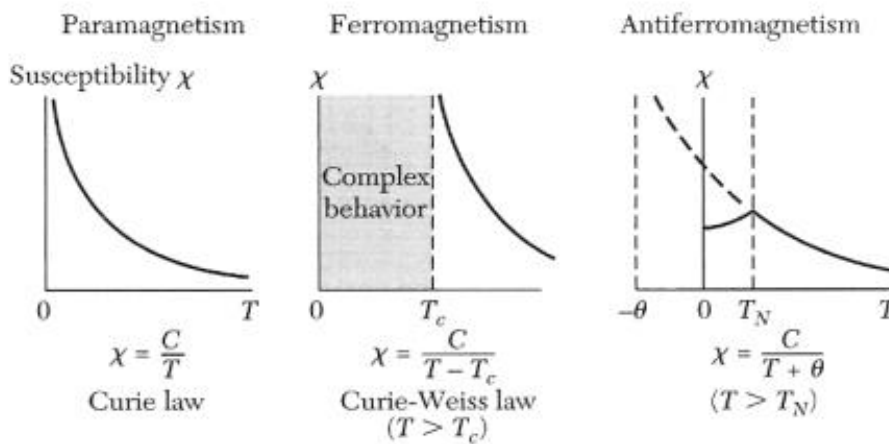


Fig.2: Behavior of magnetic susceptibility in function of temperature for magnetic phases Paramagnetism, Ferromagnetism and Antiferromagnetism. Below we see the description of Curie law and Curie-Weiss law, being C the Curie constant, T_c the critical temperature, T_N the Néel temperature (critical temperature for Antiferromagnets) and θ the Curie-Weiss temperature. Here, the "complex behavior" indicates the absence of a single model to describe the behavior below critical temperatures of ferromagnets. [1]

As we can notice above, the dependence of the magnetic susceptibility with temperature occurs until a critical temperature, following the Curie-Weiss law for ferromagnets and antiferromagnets; For paramagnets, the dependence occurs along all the range of temperature, following the Curie law.

2.3 Interactions

2.3.1 Crystal field theory

The crystal field is an electrostatic field resulting from the interactions between orbitals of neighboring ions, which may change the directions of the orbital angular momentum; In contrast with the configuration for a single atom, in a crystal we have sets of energy levels generated by lobes of charge that point towards the atoms with higher energy inside the lattice. The different crystal field levels can hold thermal excitations at moderate temperatures. [2] We usually observe this interaction in the iron group ions because the 3d lattice responsible for the paramagnetic behavior is the last one, more exposed to the crystal field. The interaction between these ions may result in the disruption of the coupling between vectors \mathbf{L} and \mathbf{S} , and the loss of accuracy of J . [1]

2.3.2 Short-range and long-range interactions

With a good approximation, the molecular field theory states the presence of an internal magnetic field \mathbf{H}_m , which holds a dependence with the critical temperature T_c above which there's no longer spontaneous magnetization, as we can see below:

$$gS\mu_B\mathbf{H}_m = k_B T_c$$

(15)

On the other hand, the trouble with the molecular field theory is that it almost neglects the short-range interactions, therefore being insufficient whilst studying interactions in an atomic level.

Now, expanding the interactions to the non-magnetic and long-ranged ones, we must mention the dipole-dipole interaction. Given the magnetic moment $\boldsymbol{\mu}$, we can write the Hamiltonian for dipole-dipole interactions as:

$$\mathcal{H}_{dipolar} = \sum_{\substack{i,j \\ i \neq j}} \left[\boldsymbol{\mu}_i \cdot \frac{\boldsymbol{\mu}_j}{r_{ij}^3} - 3(\boldsymbol{\mu}_i \cdot \mathbf{r}_{ij})(\boldsymbol{\mu}_j \cdot \mathbf{r}_{ij})/r_{ij}^5 \right]$$

(16)

This relation shows us that the bigger the spin moment is, the bigger will be the strength of the interaction. Also, it states that it is anisotropic and long-ranged for its dependence with \mathbf{r}^{-3} .

In a quantum mechanical approach, the relative direction between two interacting spins depends on the charge distribution on the system, which in its turn results from Coulomb electrostatic interactions; Therefore the spin dependent term of the Hamiltonian is proportional to the product $\mathbf{S}_1 \cdot \mathbf{S}_2$ as we show below:

$$\mathcal{H}_{spin} = -2J_{12}\mathbf{S}_1 \cdot \mathbf{S}_2 \quad (17)$$

Where we define the exchange constant as the difference between the energy of the singlet state E_S and triplet state E_T :

$$J_{12} = \frac{E_S - E_T}{2} = \int \psi_a^*(\mathbf{r}_1)\psi_b^*(\mathbf{r}_2)\mathcal{H}\psi_a(\mathbf{r}_2)\psi_b(\mathbf{r}_1)dV_1dV_2 \quad (18)$$

And ψ_a and ψ_b represents two single electron states with spatial coordinates \mathbf{r}_1 and \mathbf{r}_2 . These are denominated as the direct exchange interactions.

A particularity while working with an antiferromagnetic system is that we can't define a Hamiltonian that describes it, since we have to handle the complexity of working with two lattices. In the absence of an external field, the Hamiltonian will be given by:

$$\mathcal{H} = \frac{1}{2} \sum_{\mathbf{r}, \mathbf{r}'} |J(\mathbf{r} - \mathbf{r}')| \mathbf{S}(\mathbf{r}) \cdot \mathbf{S}(\mathbf{r}') \quad (19)$$

If we consider the system as a classic one, we can define as the lower (fundamental state) and higher value of energy for an antiferromagnetic system:

$$-\frac{1}{2} \mathbf{S}(\mathbf{S} + 1) \sum_{\mathbf{r}, \mathbf{r}'} |J(\mathbf{r} - \mathbf{r}')| \leq \mathcal{H}_0 \leq -\frac{1}{2} S^2 \sum_{\mathbf{r}, \mathbf{r}'} |J(\mathbf{r} - \mathbf{r}')| \quad (20)$$

As observed by Heisenberg, since the 3D configuration for a many-body system can be reduced to the analysis of the interactions between two neighboring atoms, the spin Hamiltonian can be written as follows:

$$\mathcal{H}_{\text{Heisenberg}} = -\sum_{ij} J_{ij} \mathbf{S}_i \cdot \mathbf{S}_j$$

(21)

In this model, we apply another approximation where $J_{ij}=J$ only for nearest neighbors and zero otherwise. What classifies the exchange interactions as direct or indirect is the distance between the electrons and the presence of an intermediate between them.[9] Now, resuming and expanding the simplest case of a Heisenberg Hamiltonian:

$$\mathcal{H} = -2 \sum \{ J_{xy} (S_{ix} S_{jx} + S_{iy} S_{jy}) + J_z S_{iz} S_{jz} \}$$

(22)

For the Heisenberg model, $J_{xy}=J_z$; For the Ising model, $J_{xy}=0$ and finally for the XY model, $J_z=0$. The Heisenberg model requires a highly symmetric system while the Ising model depends upon a large anisotropy. This is due to the constraints imposed by the crystal field. [2]

2.4 Magnetic Frustration

Magnetic frustration arises when the spin orientation cannot find a way to minimize the energy of a system through its interaction with all and each of the neighbouring spins, that is, each pair of spin cannot satisfy simultaneously a configuration of minimal energy of the system. In a more general way, we can say that a system is frustrated whenever the minimum energy of the system doesn't correspond to the minimum of all local interactions. This phenomenon can be caused by competing interactions or by the lattice structure, which is the special case denominated geometrical frustration. Frustration in a system of spins can offer interesting material of study for statistical mechanics. [3]

A simple model to illustrate geometrical frustration is a triangular disposition of antiferromagnetic Ising spins; As we can see in fig.3 below, it's impossible for the third spin to satisfy simultaneously both interactions so we entitle it as frustrated.

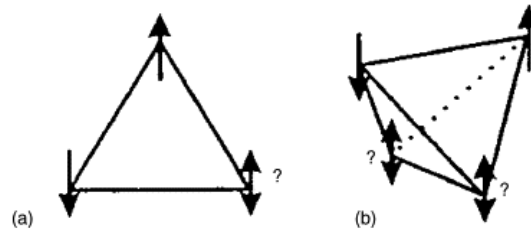


Fig.3: Geometrically frustrated system, where Ising spins can't find a single antiferromagnetic configuration of minimal energy in (a) 2D and (b) 3D configurations [3]

We can also notice on the image above that there are many possible configurations with the same ground state energy; Hence a frustrated system is characterized by a high degeneracy of the ground state. These high levels of degeneracy may result in peculiar arrangements of long-range and local ordering. We can mention spin ice, spin liquid and spin glass as some unique examples of local ordering. [3]

As for the varieties of lattices characterized by geometrical frustration, we can mention the Kagomé and Pyrochlore lattices, shown in the fig.4 – the last one will be discussed deeply in the next subsection for its relevance to this work.

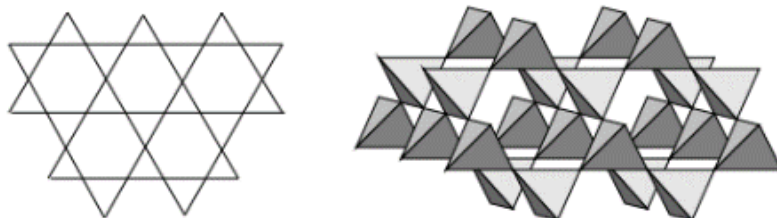


Fig.4: Kagomé and Pyrochlore lattices, from left to right. [4]

Another interesting structure is the one called Spin-Ice, a configuration similar to the oxygen atoms in ice, where we see an oxygen atom in each vertex of a tetrahedron; There, we have two hydrogen atoms closer and the other two, more distant for each atom of oxygen, as we see in the fig.5 below.

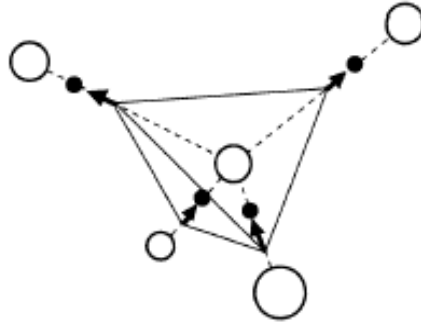


Fig.5: configuration of hydrogen (black circles) and oxygen atoms (white circles) in ice, analogous to the “two in-two out” system of spins pointing inside and outside the tetrahedra configuration, as noticed by Pauling. [7]

This configuration is called “two in-two out” or “ice rules”, which contemplates the ground state configuration of ferromagnetic spins in a pyrochlore lattice. The high degeneracy of this structure results in a finite entropy as it is cooled until temperatures close to zero Kelvin. We started to talk about a residual entropy then, a concept that seems to be in contradiction with the third law of thermodynamics. Later on, Pauling explained that this residual entropy was a result from the configurational disorder of protons in this structure.

Frustration can be analysed quantitatively by the frustration index f , defined as below:

$$f \equiv \frac{|\theta|}{T_C} \quad (23)$$

Where θ is the Curie-Weiss temperature and T_C , the critical temperature. [4] In a frustrated system, $\theta \gg T_C$, while in a system without frustration, both temperatures will be similar and the frustration index will be close to 1. We can see both temperatures indicated in the fig.6 showing the behaviour of the inverse of susceptibility of an antiferromagnet.

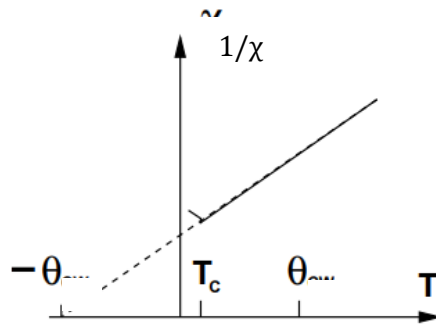


Fig.6: Behaviour of the inverse of susceptibility for an antiferromagnet. We can also notice where the characteristic temperatures θ and T_c occur. [4]

2.4.1 The pyrochlore lattice

The pyrochlore lattice (space group $Fd-3m$) is chemically composed by a sublattice of trivalent rare-earth ion, A, and a sublattice of tetravalent transition metal ion, B, in a way that it results in the formulation $A_2B_2O_7$ of corner-shared tetrahedra, as we can see below, in fig.7 :

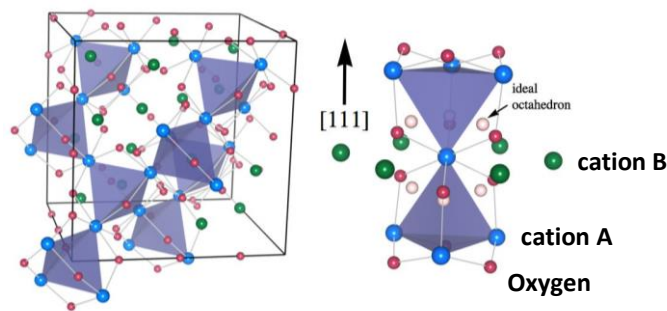


Fig.7: the pyrochlore lattice of corner-shared tetrahedra: here, we see the tetrahedra composed by the cations A (blue circles) only while cations B (green circles) are not connected as tetrahedra. The Oxygen atoms are represented by red circles. We can easily spot the presence of symmetry along the direction (111) , the diagonal of the cube. [5]

In this work, we focused our attention specially on pyrochlore structures with titanium as a transition metal base. This is due to the fact that the scientific community has been observing unique characteristics displayed by titanates at very low temperatures for the past few years (we can mention the most recent cases of $Dy_2Ti_2O_7$ and $Er_2Ti_2O_7$, for example).

Lanthanides (or rare-earth ions) attract much interest from the chemist community for properties such as its high coordination number, the wide variety of geometries, the regular decrease of radius with the atomic number and finally the magnetic properties conditioned by the number of electrons in the 4f lattice. [2] The magnetic properties also vary considerably with the atomic number (therefore with its radius) while chemical properties are very similar, since the electronic configuration is $5s^25p^6$. [1] For the purposes of this work, it's clear that our interest revolves around the last characteristic.

2.4.2 The perovskite lattice

Another lattice studied in this work is the perovskite lattice, which is also characterized as a highly symmetric structure with general formulation ABO_3 (fig.8). This structure is highly explored for its ferroelectricity properties. Notice that in the present work, we discuss a similar structure denominated as “layered perovskite” (LP), for its monoclinic configuration and therefore, highly asymmetry.

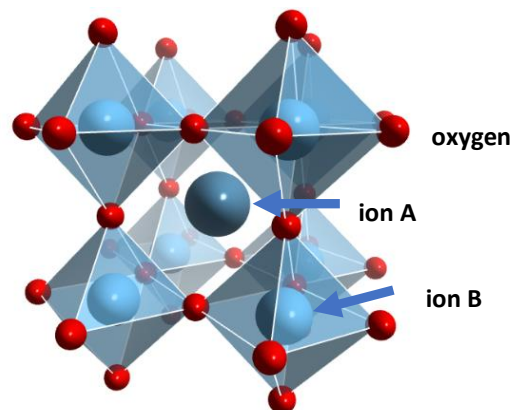


Fig.8: the perovskite lattice of octahedra. Here we can observe eight octahedra with oxygen in its corners with ion A trapped inside and ion B inside each octahedra. [6]

It's interesting to notice that the difference between the radius of ions A and B will determine the lattice: for similar radius, we will have a pyrochlore lattice while for a bigger difference of radius, we will have a layered perovskite type of lattice. [7]

Chapter 3

Specific Heat

The specific heat is one of the most informative properties of a substance. It tells us the amount of energy needed to increase the temperature of a material i.e. the excited states of a material in a certain range of temperature.

In this section, we will look into the contributions to the specific heat in a solid, focusing on the behaviour of each contribution to the heat capacity data.

3.1 Fundamental Concepts

A general way of determining the specific heat whilst holding constant arbitrary properties x, y, \dots is:

$$c_{x,y,\dots} = \lim_{dT \rightarrow 0} \left(\frac{dQ}{dT} \right)_{x,y,\dots} \quad (24)$$

Where, as a result of the first and second laws of thermodynamics, we can define the microscopic amount of heat dQ , respectively, by the following equations:

$$dQ = dE + dW \quad (25)$$

$$dQ = T dS \quad (26)$$

Where dE is the microscopic variation of energy of the system, dW the microscopic variation of work and dS , the microscopic variation of entropy. Combining them both, we get the expression for the internal energy:

$$dE = T dS - P dV \quad (27)$$

It is worthwhile to notice that ideal fluids obey the following equation of state:

$$f(P, V, T) = 0$$

(28)

Thus if we keep either P or V constant, we will obtain the two well-known heat capacities:

$$C_P = \left(\frac{dQ}{dT} \right)_P = T \left(\frac{\partial S}{\partial T} \right)_P$$
$$C_V = \left(\frac{dQ}{dT} \right)_V = T \left(\frac{\partial S}{\partial T} \right)_V \quad (29)$$

Although solids require work to maintain/change shape and dimensions, it can be shown that we can use these expressions in the case of solids without loss of generality. [8]

3.2 Heat Capacity Modes of Thermal Energy

The heat capacity is a result of the energy contribution from the various constituents of a system; For instance, whilst for a molecule in a gas we must consider rotational, translational and even molecular modes of thermal excitation, for an atom in a solid, it can only vibrate around its position in the lattice, which will originate the lattice mode of thermal excitation. Farther there are the electronic contribution, which results from thermal excitation of the free electrons on the lattice, the magnetic contribution, which we will see in more detail further in this chapter, and the nuclear contribution, which arises from the energy levels of nuclear dipoles and quadrupoles. [8]

The trouble with the measured heat capacity is that it is a sum of these contributions, which are usually hard to distinguish. One way of doing it is studying the temperature range in which each contribution operates and how it varies with it.

3.2.1 The Lattice Heat Capacity

In a lattice configuration, a simple vibration of one atom can disturb the motion of the nearest neighbourhood atoms; This circumstance must be considered due to the statistical probability of vibration prevailing at any temperature greater than zero. The lattice specific heat behaviour has been studied by the Debye's relation for phonons which had proved to be a good approximation:

$$C_v = 9rNk_B \left[\frac{4T^3}{\theta_D^3} \int_0^{\theta_D/T} \frac{x^3 dx}{e^x - 1} - \frac{\theta_D/T}{e^{\theta_D/T} - 1} \right] \quad (30)$$

Where N is the Avogadro number and θ_D is the temperature of Debye, for which every mode is excited; We can approximate the integrand as the following:

$$C_v = 3rR \left[1 - \frac{1}{2\theta} \left(\frac{\theta_D}{T} \right)^2 + \dots \right] \text{ for } T \gg \theta_D \quad (31)$$

$$C_v = \frac{12}{5} rR\pi^4 \left(\frac{T}{\theta_D} \right)^3 \text{ for } T < \theta_D/10 \quad (32)$$

Where R is the ideal gas constant. The equation above proves to work well at low temperatures for most of the substances. From that we say there is a T^3 -behaviour of the lattice specific heat at sufficiently low temperatures. [8]

3.2.2 The Electronic Heat Capacity

If we consider the model of Fermi-Dirac for a gas of electrons, we have the probable number of particles in the state ϵ_k :

$$N_k = \frac{g_k}{\exp[(\epsilon_k - \epsilon_F)/k_B T] + 1} \quad (33)$$

Here, g_k is the number of levels with energy ϵ_k and ϵ_F is the Fermi energy. This work is a good model since the electrons are indistinguishable and obey the Pauli exclusion principle. It is also suitable for short-range forces resulted from the shielding of each electron by a nearby polarization cloud of electrons.

To proceed with the calculations, it is worth acknowledging the expressions for the Fermi-Dirac function and the allowed states, respectively:

$$f(\varepsilon) = \frac{1}{1 + \exp[(\varepsilon - \varepsilon_F)/kT]}$$

(34)

$$V\mathfrak{N}(\varepsilon)d\varepsilon = 2\pi(2m)^{3/2} \frac{V}{h^3} \varepsilon^{1/2} d\varepsilon$$

(35)

Where m is the electron mass, V the volume of the system, h the Planck constant and the total number of states can be easily derived if we see that, at 0K, all states below ε_k are occupied by two electrons of opposite spins:

$$N = \frac{8}{3}\pi(2m)^{3/2} \frac{V}{h^3} \varepsilon_F^{3/2}$$

(36)

Now, the energy per mole of an electronic system is given by

$$E = 2V \int_0^\infty \varepsilon f(\varepsilon) \mathfrak{N}(\varepsilon) d\varepsilon$$

$$= E_0 + \frac{1}{3} \pi^2 V (kT)^2 \mathfrak{N}(\varepsilon_F)$$

(37)

Being the molar density of states:

$$V\mathfrak{N}(\varepsilon_F) = \frac{2\pi m}{h^2} \left(\frac{3NV^2}{\pi} \right)^{1/3} T \quad (38)$$

We can write the electronic heat capacity as the following:

$$C_e = \frac{4\pi^3 m k^2}{3h^2} \left(\frac{3NV^2}{\pi} \right)^{1/3} T$$

$$= \gamma T \quad (39)$$

Where we name the set of constants as γ . However, the measurement of the electronic heat capacity is not trivial, since its contribution is usually overshadowed by the lattice

contribution; It was observed that only at liquid-helium temperatures the data was noticeable, since it only decreases with T in contrast with the T^3 decrease of the lattice heat capacity at low temperatures. Thus, at liquid-helium temperature, we can adjust the function

$$C = \beta T^3 + \gamma T \quad (40)$$

Where β is an arbitrary constant and a plot of C/T X T^2 should give a straight line that will show the lattice region of contribution. The γ parameter depends on the band structure of the material. [8]

3.2.3 The Magnetic Contribution to Heat Capacity

At sufficiently low temperatures, the exchange interactions can surpass the random arrangement caused by the thermal energy. As we have seen in more detail in the previous section, there are more than one possible ordered state and those states are only attained in the absence of thermal agitation. Therefore at any temperature greater than zero, there will be an energy distribution that will lead to a sinusoidal orientation of the spins, which can be studied through the Fourier series, as portrayed below, in fig.9:

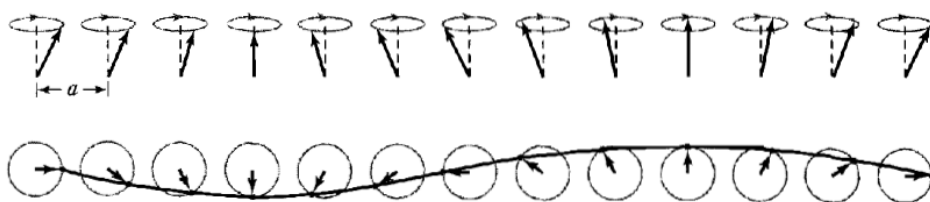


Fig.9: Spin wave configuration viewed from perspective and from above. This behavior occurs at presence of any thermal agitation in the system. [1]

Likewise the phonon analogy made in order to facilitate the mathematical analysis of the lattice configuration, we quantize spin waves into magnons, which allows us to apply Bose-Einstein statistics.

The spins in a magnetic system, following the presence of an effective field \mathbf{H}_{eff} , will obey the following Hamiltonian:

$$\mathcal{H}_i = -g\beta\mathbf{s}_i \cdot \left(\mathbf{H}_0 + \frac{2J}{g\beta} \sum_j \mathbf{s}_j \right) = -g\beta\mathbf{s}_i \cdot \mathbf{H}_{eff}$$

(41)

Where the sum covers only the two nearest neighbors and the spins will suffer a torque that can be described by

$$\frac{d(\hbar\mathbf{s}_i)}{dt} = \gamma\hbar\mathbf{s}_i \times \mathbf{H}_{eff}$$

(42)

And γ is the magnetomechanical ratio. Working with both equations, we come to the angular velocity of precession ω' :

$$\omega' = \gamma H_0 + \frac{2J}{g\beta} s q^2 a^2$$

(43)

Where γH_0 is the Larmor frequency of the spin, q a wave vector and a , the distance between two atoms. The frequency of the spin wave is given by

$$\omega = \frac{2J}{\hbar} s a^2 q^2$$

(44)

In the case of ferromagnets and ferrimagnets, the dependence in q^2 prevails; In antiferromagnets, on the other hand, this dependence is linear. From that expression, we can write for the energy in a ferromagnetic system:

$$\begin{aligned} E &= 4\pi V \int \frac{(2\alpha_f J s a^2 q^2) q^2 dq}{\exp(2\alpha_f J s a^2 q^2 / k_B T) - 1} \\ &= 4\pi V (2\alpha_f J s a^2) \left(\frac{k_B T}{2\alpha_f J s a^2} \right)^{5/2} \int \frac{x^4 dx}{e^{x^2} - 1} \end{aligned}$$

(45)

Where α_f is a constant that depends on the crystal structure and the integral above can be solved in a good approximation for low temperatures, which allows us to obtain for specific heat the following expression:

$$C_M = \frac{dE}{dT} = c_f N k \left(\frac{k_B T}{2J_s} \right)^{3/2} \quad (46)$$

Where c_f is also a constant that depends on the crystal structure; This results in the general expression for specific heat at low temperatures:

$$C_v = \gamma T + \beta T^3 + \delta T^{3/2} \quad (47)$$

It is worth to point that the heat capacity at low temperatures will be dictated by the lowest power of T ; In the case of ferrimagnets, which are insulators, there's no linear dependence in T and the dominating part will correspond to the spin wave.

For an antiferromagnetic system, we have:

$$\begin{aligned} E &= 4\pi V \int \frac{2\alpha_a J' s a^2 q^3 dq}{\exp(2\alpha_a J' s a^2 q/kT) - 1} \\ &= 4\pi V (2\alpha_a J' s a^2) \left(\frac{kT}{2\alpha_a J' s a^2} \right)^4 \int \frac{x^3 dx}{e^x - 1} \end{aligned} \quad (48)$$

And the specific heat:

$$C_M = c_a N k \left(\frac{kT}{2J'_s} \right)^3 \quad (49)$$

Here, J' is the magnitude of the exchange constant and c_a , a constant that depends on the crystal structure. The same dependence with T^3 found for the lattice contribution makes it difficult to analyze both contributions separately; An efficient way explored in this work is measuring a similar compound, subtracting its data from the first ones, which has proven to be a good approximation to work solely with the magnetic data.

Notice that from the T^3 dependence of magnetic heat capacity in the antiferromagnetic system we can derive the magnon velocity v_{mag} , an additional parameter for characterization:

$$C_M = \Lambda T^3 \quad (50)$$

$$\Rightarrow v_{mag} = \left(1537 \cdot \frac{a^3}{\Lambda}\right)^{\frac{1}{3}}$$

(51)

Where a is the lattice parameter, in Å.

3.2.4 The Schottky Effect

A notable cause of maximum in the heat capacity which was not yet elaborated in this work is the Schottky Effect. Considering an energy gap of Δ between two levels, for $T \ll \Delta/k_B$, the upper level will not be populated but for $T \gg \Delta/k_B$, both levels will be equally populated. In this interval of temperature, a quick change of energy will occur and it will be noticeable on the heat capacity data as a maximum, usually overshadowed by the other contributions mentioned so far.

For the calculation of the model for the Schottky Effect, we apply the statistical mechanics probability of a particle occupying the r^{th} level considering a group of particles with energies $\varepsilon_1, \varepsilon_2, \dots, \varepsilon_m$ with degeneracies g_1, g_2, \dots, g_m , respectively:

$$E = \frac{N \sum_{r=0}^m \varepsilon_r g_r \exp(-\varepsilon_r/kT)}{\sum_{r=0}^m g_r \exp(-\varepsilon_r/kT)}$$

(52)

Simplifying for the case of a two-level system, we have for the Schottky heat capacity:

$$\begin{aligned} C_{Schottky} &= \frac{N \varepsilon_1^2 g_0}{kT^2 g_1} \frac{\exp(\varepsilon_1/kT)}{[1+(g_0/g_1)\exp(\varepsilon_1/kT)]^2} \\ &= R \frac{\Delta^2}{T^2} \frac{\exp(\Delta/T)}{(1+\exp(\Delta/T))^2} \end{aligned} \quad (53)$$

Being R the gas constant and Δ the energy separation given in Kelvin. And the general case, considering all levels of energy, is:

$$C_{Schottky} = T \frac{d^2(RT \ln z)}{dT^2} = RT^{-2} \frac{d^2 \ln z}{d\left(\frac{1}{T}\right)^2}$$

(54)

Being $z = \sum g_r \exp\left(-\frac{\epsilon_r}{kT}\right)$. [8]

When the nucleus has a magnetic moment or even a quadrupole moment, the interaction with neighbouring atoms will lead to level splittings and the change in the population of these levels will be observed as a nuclear Schottky effect. It is once again overshadowed by other contributions to heat capacity, since the nuclear moments are much smaller than the electronic moments and may be observed in the 10^{-2} K region. On the other hand, it may also arise in diamagnetic materials. [8]

Chapter 4

An Introduction to Crystallography

The main characteristic when studying solids classified as crystalline is the periodic feature of these kind of structures, which allows us a better observation of electronic aspects, such as the specific heat and the electric conductivity. Max von Laue first identified such periodic nature through an X-Ray diffraction experiment in 1912, in which the presence of patterns corresponding to each surface of a given crystal was verified. Analyses of these patterns are, still nowadays, the major instrument for a better understanding of crystal structures.

The field of solid state physics has started being developed with the breakthrough of X-Ray diffraction in crystals, establishing itself with the arise of a quantum approach of crystallography, and it is nowadays the most well-developed area of condensed matter field.[9]

4.1 The Crystal Lattice

Whilst studying the properties of the crystal lattice, there are some useful nomenclatures which we may revise now:

4.1.1 The Bravais Lattice

The Bravais lattice, or direct lattice, is a set of mathematical points (also known as basis) composed by a configuration of atoms, molecules or ions that repeats itself along the entire lattice and can be defined through a sequence of vector translations expressed by

$$\mathbf{R} = n_1 \mathbf{a}_1 + n_2 \mathbf{a}_2 + n_3 \mathbf{a}_3. \quad (55)$$

Being \mathbf{a}_n primitive vectors which can also define the crystalline axis, it is fundamental for this arrangement to keep its symmetry by any point of view.

There are fourteen lattice types which are grouped into seven systems, classified according to the relation between its conventional axes and angles, as we see in the table 1:

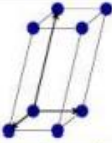
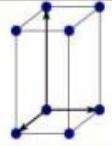

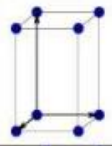
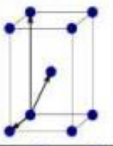
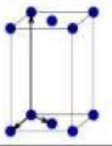
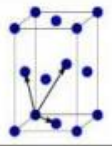
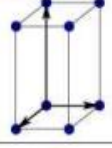

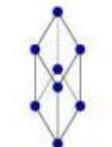
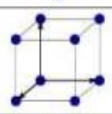
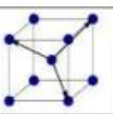
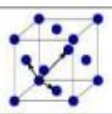
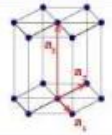
Bravais lattice	Parameters	Primitive (P)	Body centered (I)	Base centered (C)	Face centered (F)
Triclinic	$a_1 \neq a_2 \neq a_3$ $\alpha_{12} \neq \alpha_{23} \neq \alpha_{31}$				
Monoclinic	$a_1 \neq a_2 \neq a_3$ $\alpha_{23} = \alpha_{31} = 90^\circ$ $\alpha_{12} \neq 90^\circ$				
Orthorhombic	$a_1 \neq a_2 \neq a_3$ $\alpha_{12} = \alpha_{23} = \alpha_{31} = 90^\circ$				
Tetragonal	$a_1 = a_2 \neq a_3$ $\alpha_{12} = \alpha_{23} = \alpha_{31} = 90^\circ$				
Trigonal	$a_1 = a_2 = a_3$ $\alpha_{12} = \alpha_{23} = \alpha_{31} < 120^\circ$				
Cubic	$a_1 = a_2 = a_3$ $\alpha_{12} = \alpha_{23} = \alpha_{31} = 90^\circ$				
Hexagonal	$a_1 = a_2 \neq a_3$ $\alpha_{12} = 120^\circ$ $\alpha_{23} = \alpha_{31} = 90^\circ$				6

Table 1: Bravais lattices according to lattice parameters of angle and axes. Modified from [9].

4.1.2 The Primitive Unit Cell

The primitive unit cell is a unit of volume that can fill up the Bravais lattice alone through translation operations. It is defined by the same primitive vectors \mathbf{a}_n by:

$$V_c = |\mathbf{a}_1 \cdot \mathbf{a}_2 \times \mathbf{a}_3|. \quad (56)$$

We also have the unit cell and the Wigner-Seitz cell as other common choices of usage.

4.1.3 The Reciprocal Lattice

For a given plane wave $e^{i\mathbf{k}\cdot\mathbf{r}}$, the set of all wave vectors \mathbf{K} which results in plane waves with the same periodicity of the Bravais lattice is called its reciprocal lattice. Being \mathbf{R} vectors in the Bravais lattice as defined in (55), it assures the following algebraic condition:

$$\begin{aligned} e^{i\mathbf{K}\cdot(\mathbf{r}+\mathbf{R})} &= e^{i\mathbf{K}\cdot\mathbf{r}} \\ \Rightarrow e^{i\mathbf{K}\cdot\mathbf{R}} &= 1 \end{aligned} \quad (57)$$

The relation between the reciprocal lattice primitive vectors \mathbf{b}_i and the primitive vectors \mathbf{a}_n is given by:

$$b_1 = 2\pi \frac{a_2 \times a_3}{a_1 \cdot a_2 \times a_3}; \quad b_2 = 2\pi \frac{a_3 \times a_1}{a_1 \cdot a_2 \times a_3}; \quad b_3 = 2\pi \frac{a_1 \times a_2}{a_1 \cdot a_2 \times a_3}. \quad (58)$$

Notice that a crystal's diffraction pattern shows the reciprocal lattice while a microscopic image reveals the crystalline lattice. [9]

4.1.4 The Miller Index

We can define the orientation of a crystalline plane through an index system known as Miller Indices: those indices correspond to the shortest vectors of each

coordinate from the reciprocal lattice, normal to the lattice planes – which, in its turn, are separated from each other by $d = \frac{2\pi}{K}$.

Considering that the Miller Indices h, k and l are perpendicular to the reciprocal lattice vector $\mathbf{K} = h\mathbf{b}_1 + k\mathbf{b}_2 + l\mathbf{b}_3$, the last will be contained on the continuous plane $\mathbf{K} \cdot \mathbf{r} = A$; This plane crosses the primitive vectors \mathbf{a}_n axes, as shown in fig.10 below:

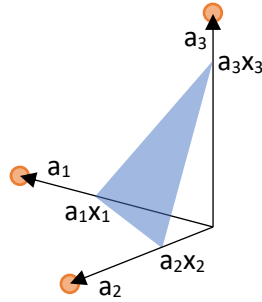


Fig.10 : Lattice plane crossing the primitive vectors axes, being \mathbf{a}_n axes and x_n points of intersection in the respective axis.

Notice that the points in the reciprocal lattice are given by the set of vectors

$$\mathbf{K} = u_1\mathbf{b}_1 + u_2\mathbf{b}_2 + u_3\mathbf{b}_3 \quad (59)$$

Where u_n are integers. From satisfying the plane equation $\mathbf{K} \cdot (x_i\mathbf{a}_i) = A$, we obtain the points of intersection x_i :

$$x_1 = \frac{A}{2\pi h}, \quad x_2 = \frac{A}{2\pi k}, \quad x_3 = \frac{A}{2\pi l} \quad (60)$$

The crystallographers establish the following proportional relation for the Miller indices:

$$h : k : l = \frac{1}{x_1} : \frac{1}{x_2} : \frac{1}{x_3} \quad (61)$$

It is useful to note that the Miller indices are represented in parentheses while the Bravais lattice directions are represented in brackets. [9]

4.2 X-Ray Diffraction

The structural analysis of crystals based on visible light reflection by the crystalline surfaces was a familiar method in experimental physics; however, real progresses only started in 1912, when Max von Laue introduced the X-Ray diffraction based upon the fact that the wavelength of the diffracted radiation must be smaller than the studied lengths, as already determined by optical geometry.

Still nowadays, X-ray diffraction is predominantly chosen to carry out crystalline structure analysis, followed by neutron and electron diffraction – each of which being more suitable for a given energy band, as we will see in the following argument. From the wavelength definition, we have:

$$\lambda = \frac{c}{\nu} = \frac{hc}{E} \quad (62)$$

Where c is the light velocity, ν is the frequency of its wave, h the Planck constant and E , the energy of the light.

The type of interaction between matter and radiation will lead to the application of a certain radiation type: electron beams can't penetrate very deep due to its highly levels of interaction with electrons of the matter, therefore being applicable only to thin films and superficial studies; X-ray diffraction, on the other hand, is only suitable for heavy atoms, since it's mainly scattered by electrons. [9]

4.2.1 Bragg Formulation

In 1913, William Lawrence Bragg established the basic conditions for the occurrence of diffraction, contemplating only the laws of geometrical optics and ignoring physical optics. In this configuration, the angle of incidence must be equal to the angle of reflection (specular reflection), as we notice in fig.11 below:

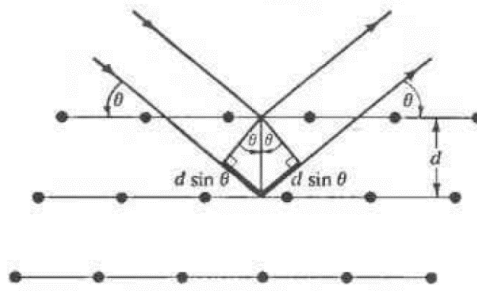


Fig. 11: Bragg formulation for reflection by two consecutive lattices separated by d . [9]

As we see above, we can expect a constructive interference when the below relation between the wave length λ and the angle of incidence θ is satisfied:

$$2d \sin \theta = n\lambda$$

(63)

This relation is known as the Bragg's law, in which n is an integer.

4.2.2 von Laue Formulation

In a more general way than the Bragg's principle, the Laue formulation doesn't assume a specular reflection but the occurrence of reflection in all directions for each site in the Bravais lattice.

In the fig.12 below, we notice that the difference in phase factors is given by $\exp[i(\mathbf{k}-\mathbf{k}')\cdot\mathbf{r}]$:

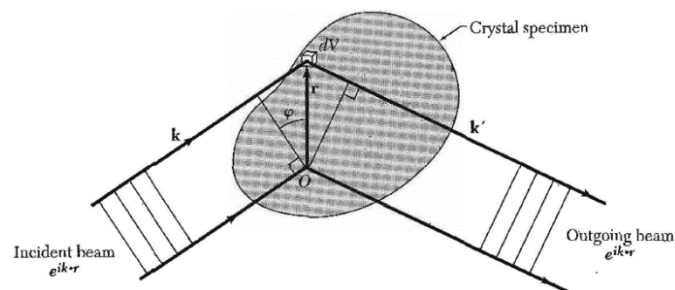


Fig.12: Geometrical condition for the occurrence of diffraction. [1]

Whilst considering the wave amplitude proportional to the electron concentration, we can obtain the amplitude of the scattered wave \mathbf{k}' in the equation below:

$$F = \int dV n(\mathbf{r}) \exp[i(\mathbf{k} - \mathbf{k}') \cdot \mathbf{r}]$$

(64)

F is known as the scattering amplitude and $\Delta\mathbf{k}$, in $\Delta\mathbf{k} = \mathbf{k}' - \mathbf{k}$, the scattering vector. $n(\mathbf{r})$ is the electron number density. Replacing $n(\mathbf{r})$ expression in (64), we have:

$$F = \sum_{\mathbf{K}} \int dV n_{\mathbf{K}} \exp[i(\mathbf{K} - \Delta\mathbf{k}) \cdot \mathbf{r}]$$

(65)

Fulfilled the condition of an elastic scattering and of the scattered vector being a vector of the reciprocal lattice, $\Delta\mathbf{k}=\mathbf{K}$, we can write a diffraction condition

$$2\mathbf{k} \cdot \mathbf{K} + K^2 = 0$$

$$\Rightarrow 2\mathbf{k} \cdot \mathbf{K} = K^2$$

(66)

as we consider $-\mathbf{K}$ also a vector of the reciprocal lattice. This expression is an alternative form of Bragg's law and can be applied as condition to the occurrence of diffraction.

Chapter 5

Recent Studies

In this chapter, we intend to discuss some of the main results found in literature concerning our samples and other pyrochlore samples with which comparison seemed to be enriching for this work.

5.1 Sample $\text{Sm}_2\text{Ti}_2\text{O}_7$

The sample of $\text{Sm}_2\text{Ti}_2\text{O}_7$ has been studied in two main articles: Singh et al. (2008) [11] and more recently by Mauws et al. (2018) [13].

In the first reference, the authors work with a single crystal sample in direction (111) obtained by the Floating Zone method. The measurements were done between the range of $T=2\text{K}$ and $T=300\text{K}$, which prevented the authors of seeing any transition peak. In sequence, the authors have analyzed the magnetization data for both crystal and powder samples, applying the susceptibility fitting:

$$\chi = \chi_{CW} + \chi_{VV} \quad (67)$$

Where χ_{CW} and χ_{VV} are respectively the Curie-Weiss susceptibility and the Van Vleck susceptibility:

$$\chi_{CW} = \frac{N_A \mu_{eff}^2}{3k_B(T-\theta)} \quad (68)$$
$$\chi_{VV} = \frac{20\mu_B^2}{7k_B\Delta_J} \quad (69)$$

N_A being the Avogadro's number, μ_{eff} the effective magnetic moment, k_B the Boltzmann constant, θ the Curie-Weiss temperature and Δ_J the intermultiplet splitting width. This is

because the ion of Sm^{3+} doesn't follow the classic Curie-Weiss law. We see a broad maximum in the susceptibility data around $T=140\text{K}$. While measuring the heat capacity between 0.5K and 300K , the authors observed a sharp increase below $T=0.5\text{K}$, which they attribute to short-range spin correlations in Sm . They weren't able to see the ordering since measurements were performed only until $T=0.5\text{K}$. The variation of entropy found was 13% less than the expected value of $R\ln 2$, which may be caused by the measurements of heat capacity stopping at $T=0.5\text{K}$.

In the second reference paper [13], the authors worked with an enriched isotope of Sm^{3+} sample (^{154}Sm) to allow the neutron diffraction analysis. There they were able to show the presence of a configuration they call all in-all out, in which we have a tetrahedron with all spins pointing in accompanied by a tetrahedron with all spins pointing out, as we see in the fig. 13.

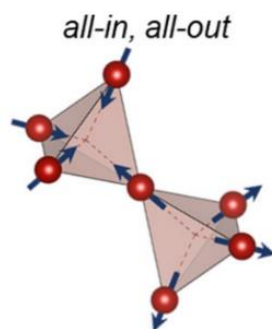


Fig.13: "all in-all out" configuration of $\text{Sm}_2\text{Ti}_2\text{O}_7$ [13].

This configuration differs from the spin ice system because the orientation of one spin in the tetrahedron constrains the orientation of all the others and results in no degeneracy. This configuration is said to be possible because of the antiferromagnetic Ising spins in addition to the minor dipolar interaction. The authors also discuss the coexistence of all in-all out state with signs of spin ice disordered at low temperatures, which is called moment fragmentation. While measuring heat capacity until low temperatures, they were also able to see for the first time the long-range magnetic ordering transition at $T_N=0.35\text{K}$.

5.2 Sample $\text{Nd}_2\text{Ti}_2\text{O}_7$

The sample of $\text{Nd}_2\text{Ti}_2\text{O}_7$ is characterized as a Layered Perovskite, a composition analogous to a asymmetric Perovskite inside the monoclinic configuration (fig.14). It was studied by Xing et al. [12] with focus on its highly anisotropic system. The authors work with a single crystal sample along the direction (100) and (001) and a powder resulted from crushing part of the single crystal sample. By taking magnetic measurements and fitting the Curie-Weiss law, it is easy to notice the high anisotropy present in the sample as well as the antiferromagnetic state. The effective moment μ_{eff} found for the three samples goes between the values 3.44-3.49 μ_{B} while the value of Curie-Weiss temperature varies a lot more between 10.4 and -128.9K. It is noticeable that the magnetization is stronger along the (001) axis, indicating this to be the easy axis of the crystal. Heat capacity was measured until 2K so the transition peak wasn't observed but a two-level Schottky model was well fitted on the data until high fields (9T).

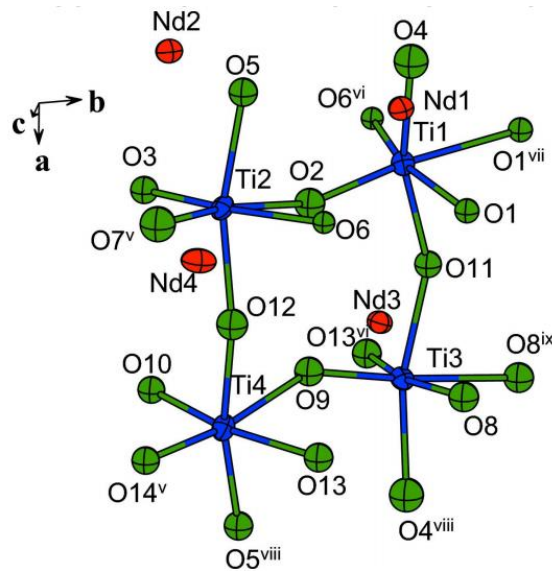


Fig.14: $\text{Nd}_2\text{Ti}_2\text{O}_7$ atomic disposition, known as “layered perovskite”(LP), where octahedra composed by oxygen atoms in its vertices and a titanium atom in its center are asymmetrically disposed, in opposition to the highly symmetric structure of perovskite, with atoms of neodymium in its surroundings. [10]

Chapter 6

Experimental Procedure

As we have seen in the previous subsections, there's a few good reasons for studying magnetic properties of titanate pyrochlores. In addition to that, there's also a very good reason to study the chosen samples of titanates $\text{Sm}_2\text{Ti}_2\text{O}_7$ and $\text{Nd}_2\text{Ti}_2\text{O}_7$. Both samples have been little explored for its low magnetic moment, in the case of Samarium sample [11], and the manifestation of magnetic ordering only at very low temperatures, in the case of both Samarium and Neodymium. [12] Besides, there're a few properties that contribute to the uniqueness of these samples, such as the already discussed moment fragmentation on the Samarium sample [13] and the high anisotropy of the Neodymium crystal.

6.1 Sample Preparation

We have worked with two varieties of samples: polycrystalline sample of Neodymium and single crystal samples of both Neodymium and Samarium. For the effect of comparison, we have studied a polycrystalline sample of Samarium crushing a piece of the single crystal. The polycrystalline sample of $\text{Nd}_2\text{Ti}_2\text{O}_7$ was obtained by the sol-gel method of synthesis, which was performed by the study group of professor Flávio Vichi and dr. Marina Leite, from the Instituto de Química at USP. The sample received thermal treatment for 2h at $1\text{k}^\circ\text{C}$, which resulted in a blue polycrystalline sample. The sol-gel method is of interest for us because it controls the surface of the samples (quantity of pores and connections developed) during the initial steps of the synthesis. [14]

Both single crystal samples were grown by professor Jason Gardner by the floating zone technique (FZ). The FZ technique consists on placing a compact of the powder sample resulted from blending correct stoichiometric amounts of each reagent in the furnace, where the sample will receive heating from two halogen bulbs and be under a controlled atmosphere of an oxygen or argon flow. This technique is very efficient to control the sample contamination, since it doesn't require the use of a vessel, and the development of bulk samples. Besides, it allows us to achieve high temperatures (<2800°C). The growth of the samples studied in this work, in particular, was done by reacting de rare earth oxide RE₂O₃ (99.9%) and TiO₂ (99.99%) at 1300°C in air for several days, following sintering of the pressed powders at 1350°C in air. The samples were than placed in a double ellipsoidal IR image furnace (NEC-N35HD) with two 3.5 kW halogen lamps, rotating at 20-30 rpm in air at ambient pressure (fig.15). [15]



Fig.15: single crystal of the sample Sm₂Ti₂O₇, with approx. 6cm of width and a diameter of 8-9mm, transparent to light with a deep red colour. [15]

The single crystal of Nd₂Ti₂O₇ was a single disk of 8-9mm of diameter and 3mm of width, also transparent to light and with a deep red colour.

6.2 X-Ray preliminary analysis

Some of the X-Ray diffraction techniques discussed on previous chapters were used to make a preliminary study of the samples, in order to check its phase and quality and to find the directions on the single crystal samples.

The X-Ray diffraction (XRD) technique, based on Bragg's principle, was applied to the powder samples as we see in fig.16 :

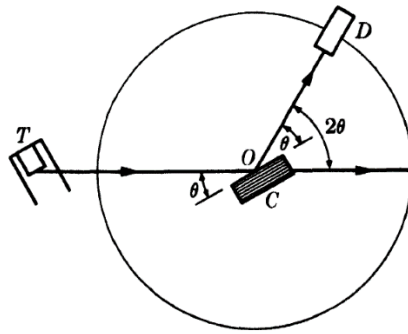


Fig. 16: X-Ray diffractometer θ - 2θ with Bragg-Brentano geometry. [16]

In the configuration above, the 2θ angle is between the incident beam and the diffracted beam that arrives at the detector. For the analysis of our samples, we worked with the diffractometer with Bragg-Brentano geometry from the group of Dr. Márcia Fantini, from the Departamento de Física Aplicada (FAP) at Universidade de São Paulo, as we see in the fig.17.



Fig.17: diffractometer theta-2theta, Bragg-Brentano geometry, at FAP (USP).

To study the single crystal samples, we used the Laue back-scattering method, as we can see in the fig.18, with a goniometer exactly as depicted in fig.19, below:

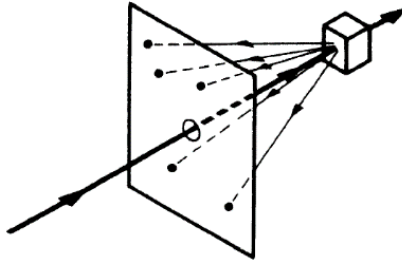


Fig.18: Laue back-scattering schematization. Here, a film is put between the sample and the incident X-Ray; The X-Ray is diffracted and forms different patterns for each crystallographic group and direction.[16]



Fig.19: triple-axis goniometer used to find the crystal directions. The sample is placed in the indicated spot while the goniometer can be moved in the three indicated directions, with a high precision. Taken from the Crystal Growth Lab (DCMPMS, TIFR) page, from Mumbai, India.

In this method, we set a film between the sample and the X-Ray source; Then we digitalise the patterns and use a software to find the correspondent lattice of the geometry studied. In this work, we chose to use the software Clip (Cologne Laue Indexation Program), which disposes of the pattern of each lattice for each space group, allowing us to fit the better pattern for the data collected.

6.3 Magnetic Measurements

We started by using a SQUID (Superconducting Quantum Interference Device) to take magnetic data, a magnetometer which operates with a precision of 10^{-7} emu and can apply a magnetic field as large as 7T and temperatures between 2K and 400K, reached with ^4He . It is composed by a closed superconducting loop with Josephson junctions, through which the sample is moved and induces a current detected by the SQUID sensor coils. The SQUID counts with a linear current to voltage converter, which allows the current detected to be proportional to the magnetic moment of the sample and the accuracy of the measured magnetic moment be very high (fig.20).



Fig.20 : 7 Tesla SQUID Magnetometer from Quantum Design (MSMS); 1.8 - 400K. AC & DC

The measurements on a SQUID can be realized in modalities DC and AC: DC measurements take place with the sample under a constant field while in AC measurements, an alternating test field is overlaid on the DC field, resulting in a magnetic moment with time dependence. The resulting field induces current on the coils without the necessity of moving the sample between them, thus eliminating any current resultant from moving the sample. We can see in fig.21 a simplified scheme of a SQUID. [17]

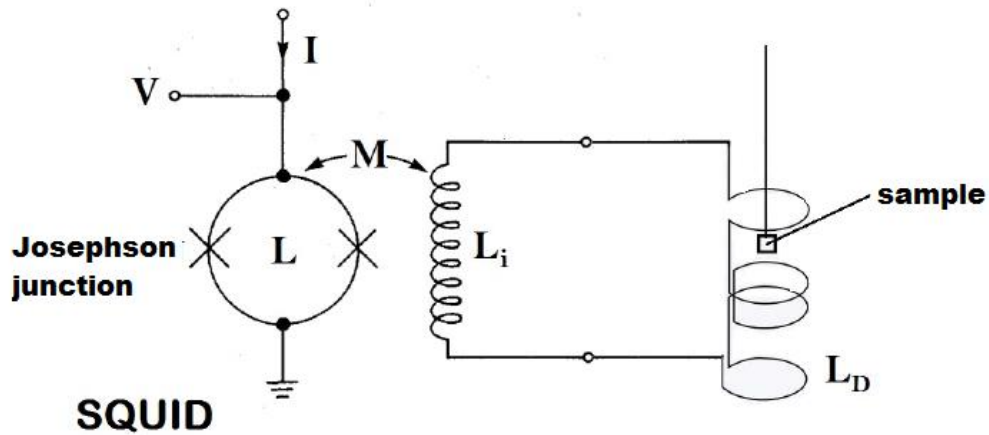


Fig. 21: simplified scheme of the SQUID (modified from [18]). L is the inductance, I the electrical current, V the voltage and M, the magnetization.

A particularly interesting measurement we do in the SQUID is the set ZFC/FC: In ZFC, we cool the sample temperature without any external field and start to measure the magnetization while we increase the temperature and insert an external field; Then we cool the sample again without turning of the external field and take the measurements. In the fig.22, we see the graph of ZFC/FC data for a generic sample.[17]

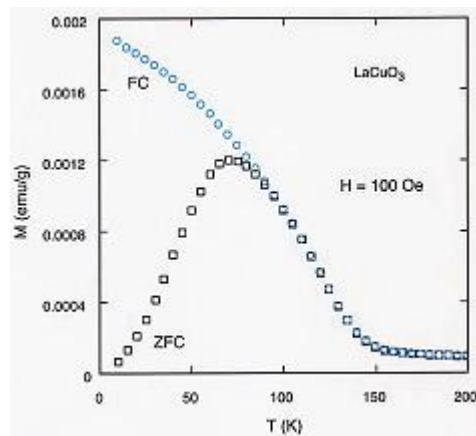


Fig.22 : ZFC and FC curves for a sample of LaCuO₃ [17].

We have also used a VSM (Vibrating Sample Magnetometer) to achieve magnetic measurements of high sensitivity, such as 10^{-5} and 10^{-6} emu, and low temperatures as 0.4K, with a pumping system of ^4He and liquid ^3He . This device operates vibrating the

sample through a spire, causing a variation of the magnetic flux and resulting in an induced current, from which we can derive the magnetic field of the sample through the following equation

$$V(t) = \sum_n \int_S \frac{dB(t)}{dt} dS$$

(70)

Where n is the number of loops of the spire and S, its area. This system requires extremely uniform magnetic fields. We can see in fig.23 below how a VSM operates: the sample in (5) vibrates parallel to the applied field generated by (1), (2) and (4); The magnetic field induces voltage in the detection coils (7), which is proportional to the magnetic moment of the sample. [19]

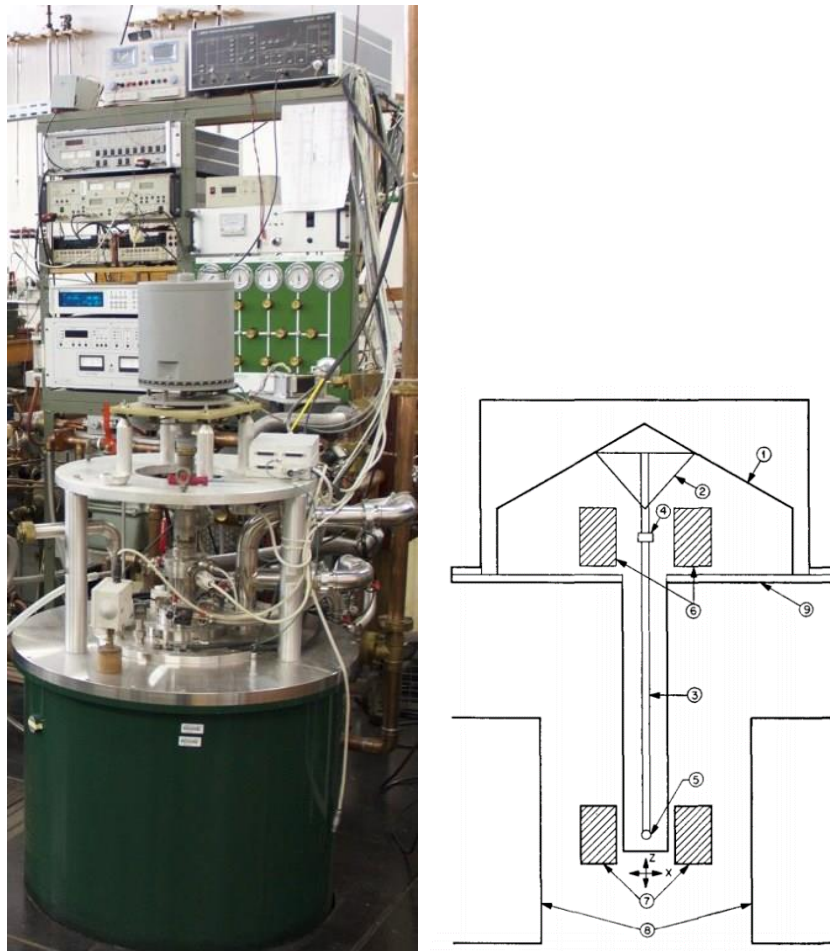


Fig. 23: VSM magnetometer with 20 T superconducting coil and He-3 Cryostat for measurements down to 0.5 T (left) followed by a simplified schematization of a VSM (right): (1) loud-speaker transducer, (2) conical paper cup support, (3) drinking straw, (4) reference sample, (5) sample, (6) reference coils, (7) sample coils, (8) magnet poles, (9) metal container. [19]

Finally, we have worked with an ac susceptometer that operates similarly to the VSM, using pickup coils to detect changes in the magnetic flux. It operates until low temperatures as 0.35K and magnetic fields of 7.5T (fig.24).



Fig.24 : 3-ac-susceptometer with 7.5 T superconducting coil and diffusion pumped He-3 glass cryostat for measurements down to 0.35 K.

The ac susceptometer is based on a primary coil that produces an ac field h_{ac} which is applied to the sample in addition to a static field H . Being $h_{ac}=h_0\cos(\omega t)$, the susceptibility will be derived by the following expression:

$$\chi = \frac{dM}{dh_{ac}} \quad (71)$$

The sample is then placed between a primary and a secondary coil, as shown in fig.25. The secondary coils are two identical pickup coils placed inside the primary one and have the function to cancel the voltages induced by the ac field. The calculation is thus made making measurements with and without the sample between the secondary coils. [20]

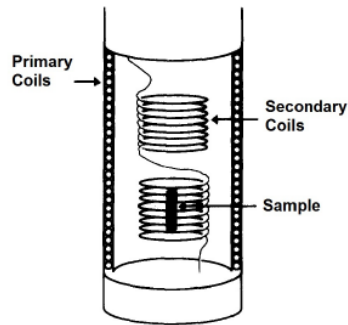


Fig.25: primary and secondary coils position inside the susceptometer. [20]

6.4 Heat Capacity Measurements

The specific heat measurements were all carried out on the PPMS (Physical Property Measurement System). It is based on observing how the amount of heat provided to (or retrieved from) the composition of sample plus a platform affects its temperature.

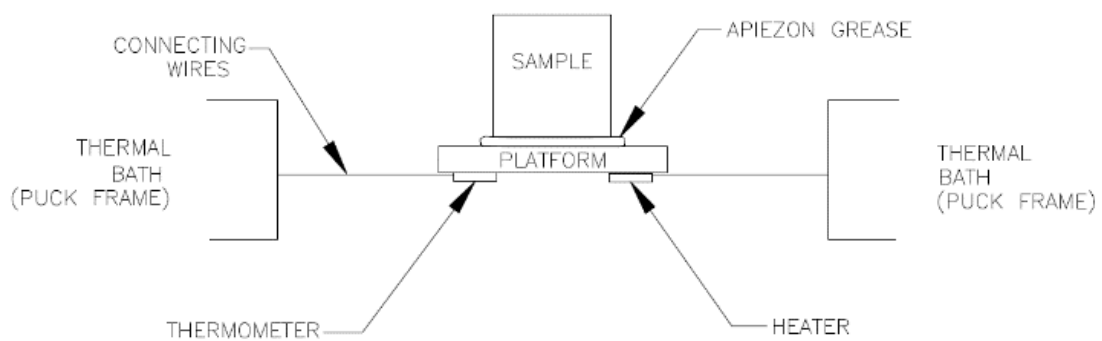


Fig.26: Sample platform schematization of the PPMS. [21]

In the fig.26 above, we can notice how small wires connect the system (heater, thermometer and platform) but the connection between the sample and the system is

given by the thin layer of grease, which assures thermal contact between them. [21]
We've also worked with a coupled a dilution refrigerator which works with the quantum properties of He isotopes: ^3He behaves as an ideal gas of reduced mass and it is pumped over the surface of liquid ^4He ; This extracts the latent heat from the liquid and allows us to arrive at very low temperatures, such as 0.05K. [22][23]

Chapter 7

Results and Discussion: $\text{Sm}_2\text{Ti}_2\text{O}_7$

In this chapter, we discuss the results obtained for the sample of samarium. The greatest interest in studying the pyrochlore $\text{Sm}_2\text{Ti}_2\text{O}_7$ is the fact that it has not been completely characterized yet, specially at low temperatures. This may be a result of its low magnetic moment (a factor of ten lower than other well-known rare-earth titanates such as $\text{Ho}_2\text{Ti}_2\text{O}_7$ and $\text{Dy}_2\text{Ti}_2\text{O}_7$, with the lowest g-factor possible for the $4f^5$ electronic configuration, $g_J=2/7$, which lead to a recent study of its isotopically enriched formulation (^{154}Sm) since the high absorption of neutrons by its natural form hindered the study through neutron diffraction [13]. Sm^{3+} ion presents another interesting feature regarding the population of state $7/2$: the population of the state changes with temperature and influence the final susceptibility data. [2] For being located between stable and heavier pyrochlore structures (structures that doesn't require the appliance of pressure during the synthesis processes in order to develop a pyrochlore structure) and monoclinic structures, it is expected that the pyrochlores of Samarium will present some valuable features in the studies of magnetic frustration.

We worked with a single sample of crystal, which we later crushed to allow us to analyse its X-Ray pattern and to confirm the absence of impurities. We were able to make measurements of heat capacity and magnetization at very low temperatures, which allowed us to see a transition peak that haven't been observed in the literature until the moment. The magnetization measurements were carried out on a Quantum Design SQUID and a VSM while the heat capacity measurements were obtained through Quantum Desgin's PPMS, sometimes with a coupled refrigerator.

7.1 Preliminary Analysis

We started our studies of sample $\text{Sm}_2\text{Ti}_2\text{O}_7$ with a single crystal sample. Knowing already that the space group of the sample is Pyrochlore ($Fd-3m$) and having [11] for comparative ground, we started by finding the directions (110) and (111) of the sample through the Laue backscattering method, being the first the direction of growth of the crystal and the second, the most symmetric direction for the Kagomé lattice. We see in fig.27 the green dots as the theoretical patterns correspondent to each direction indicated on the picture, from the software Clip, and the black dots the experimental results resulted from the Laue backscattering. The crystallographic parameters presented in ref. [11] were adopted in place of already known parameters for pyrochlore structures.

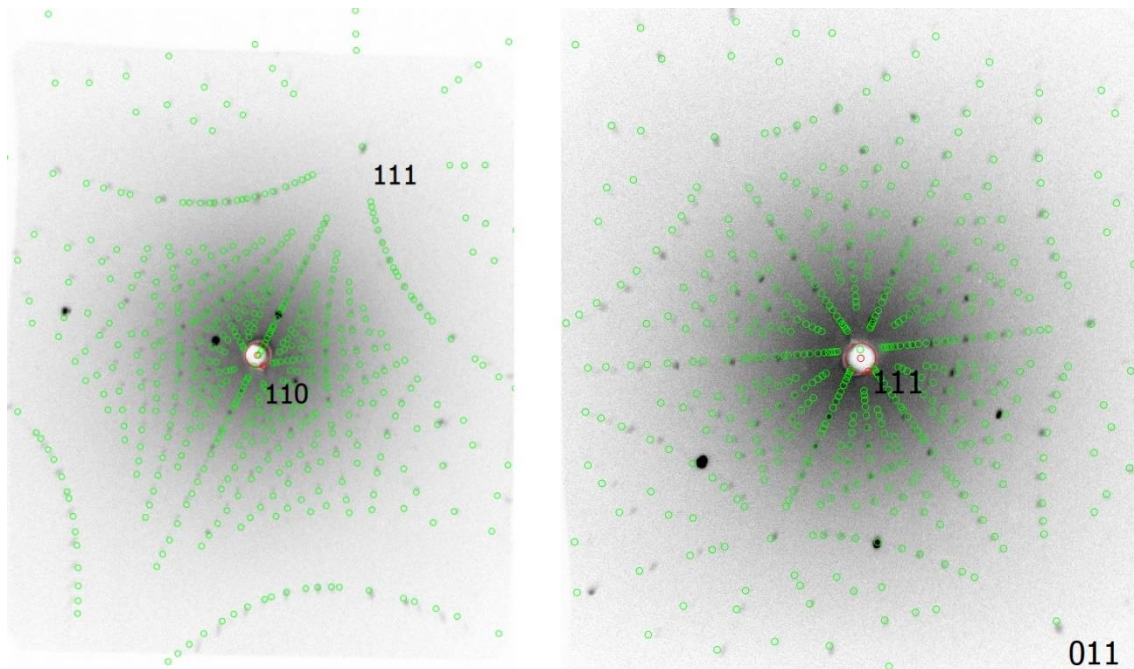


Fig. 27: diffraction pattern found for the directions (110) and (111), from left to right, with the help of software Clip.

From the first observation of these patterns, it was easy to notice the symmetry and similarity on each direction, attesting the absence of anisotropy on the sample, as expected for a cubic symmetry.

Following the single crystal orientation, we separated a piece of the sample and crushed it, which allowed us to perform the analysis of X-ray data and check the purity of the sample. We used the data found in ref. [24] to compare the localization of the peaks, overlapping both data, which certifies us about the absence of impurities, as we see in fig.28.

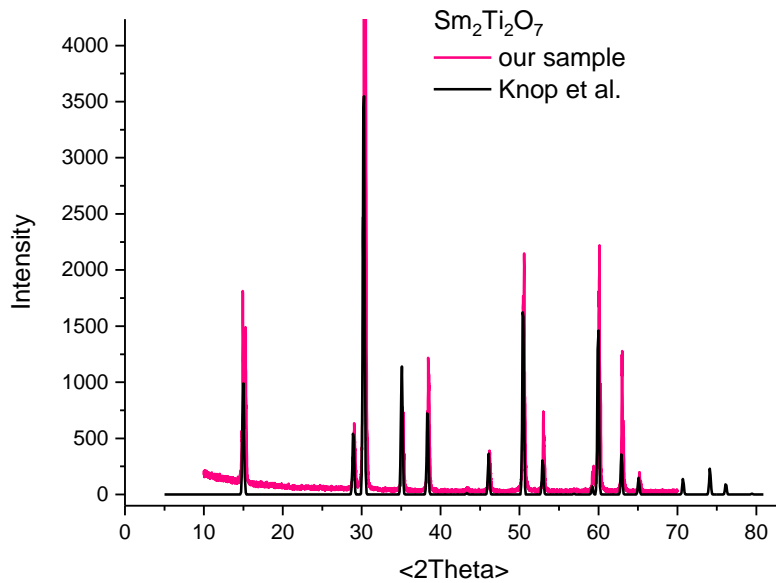


Fig. 28: X-ray diffraction data from our sample of crushed crystal (blue) and the data found in ref [24] overlapped.

Note that in order to confirm the purity of the sample and to certify the absence of structural deficiencies (such as oxygen vacancies) it is necessary to use Rietveld refinement of the data, which can be done in a future work. The difference observed in the intensity of the peaks can derive from the diffraction equipment used in both works.

7.2 Magnetic Measurements

We have started the magnetization data analysis by the ZFC and FC measurements for both orientations ((111) and (110)) of the single-crystal. We notice a classic paramagnetic behavior in the (111) direction fig. 29-a), with no clear distinction

between the ZFC and FC data, while the data in fig.29-b) presents some divergence at higher temperatures; On the other hand, it is also characterized by more noise, which may make it less credible. We have also observed an extended maximum around $T=128\text{K}$, a close enough similarity with the “broad maximum centered at $T=T_{\text{MAX}}=140\text{K}$ ” [11]. This maximum is attributed to the effect of crystalline field in the same reference, where the authors have studied the diluted sample of $\text{Sm}_{0.05}\text{Y}_{1.95}\text{Ti}_2\text{O}_7$ and assumed all the ions of Sm^{3+} as being isolated. There, a very similar maximum was observed near the temperature of maximum observed in the $\text{Sm}_2\text{Ti}_2\text{O}_7$ sample, which indicates that it is caused by the crystal field on ion Sm^{3+} .

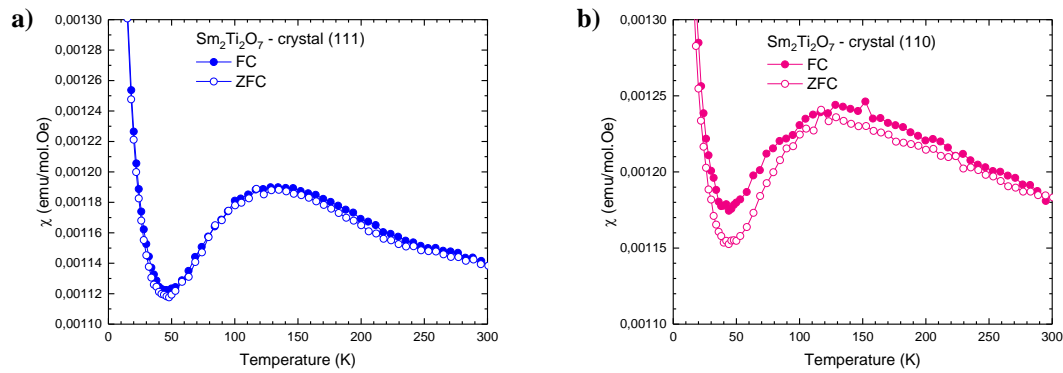


Fig. 29: ZFC and FC curves for the crystal of $\text{Sm}_2\text{Ti}_2\text{O}_7$ along the orientations **a)** (111) and **b)** (110), at a applied field of 100 Oe.

On fitting the data in a wider range, the R^2 value (fraction of the total squared error) became a bit worse. The fitting for the range proposed by the authors at (67) gave us a better R^2 value, that is the shorter range of temperature provided us a better fitting. It is important to notice here that the fitting at higher temperatures was not possible for the presence of the high crystalline field influence. The parameters derived from that can be seen at the table 2 below.

	powder	crystal (110)	crystal (111)	Singh et al. (Crystal (111))
μ_{eff}	$0.06\mu_B$	$0.06\mu_B$	$0.06\mu_B$	$0.15\mu_B$
θ	0.11K	- 0.29K	- 0.34K	- 0.26K

Table 2: parameters derived from the fitting proposed in [11] in comparison with the data presented at the same ref., for a crystal in direction (111), and our three types of sample.

We see in fig.30 that the values for μ_{eff} are coincident for our samples but they deviate from the value derived in the reference. Notice also that both values of μ_{eff} are a lot smaller than the expected value for the free ion of Sm^{3+} , $\mu_{\text{eff}}=0.83\mu_{\text{B}}$. The sample of Sm^{3+} contrasts with the other pyrochlores for its reduced value for μ_{eff} . On the other hand, the values derived for θ reassert the antiferromagnetic behaviour of the samples – they are all negative with exception to the powder value, which is very low and can be considered result from a little deviation.

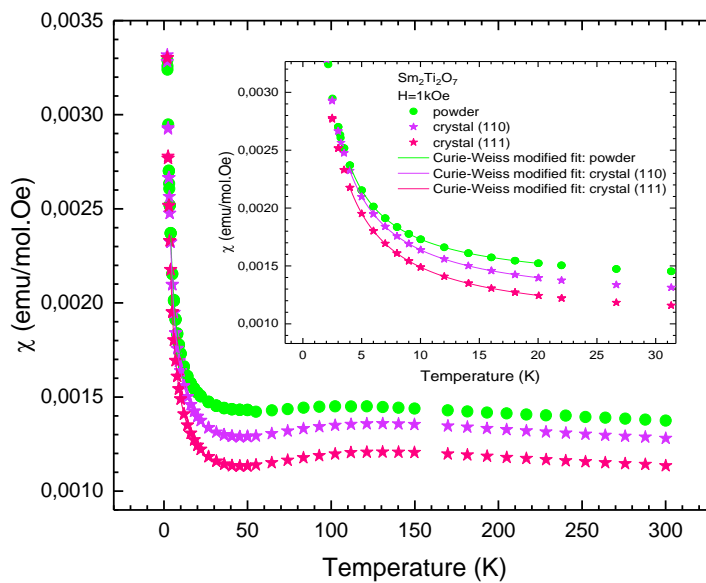


Fig.30 : Susceptibility of crystal (at (110) and (111) directions) and powder samples, with the susceptibility fitting used in Singh et al. (67) applied at the range of 4-20K, on the inset.

Finally, we can observe the presence of anisotropy at temperatures above 5K in the sample of $\text{Sm}_2\text{Ti}_2\text{O}_7$.

As we derive the frustration index for the sample of $\text{Sm}_2\text{Ti}_2\text{O}_7$, we notice that it is found between 0.31 and 0.97, close to 1. It indicates the absence of frustration in this compound.

Now, to verify the behavior of the samples at high values of field, we analyzed the behavior of magnetization in function of field for each sample at low temperature ($T=2\text{K}$) in fig.31; We've also compared this data with the one presented in ref.[11], as we can see

in the graph below. We've repeated the measurements for each sample (crushed crystal, single crystal oriented at directions (111) and (110)) seven times in order to make error bars, considering the intrinsic experimental error caused by the sample misalignment in the SQUID. Considering the error bars, we can immediately say the sample of $\text{Sm}_2\text{Ti}_2\text{O}_7$ doesn't present anisotropy at low temperatures (2K). On the other hand, we notice that our data is not compatible with the ones presented in the reference.

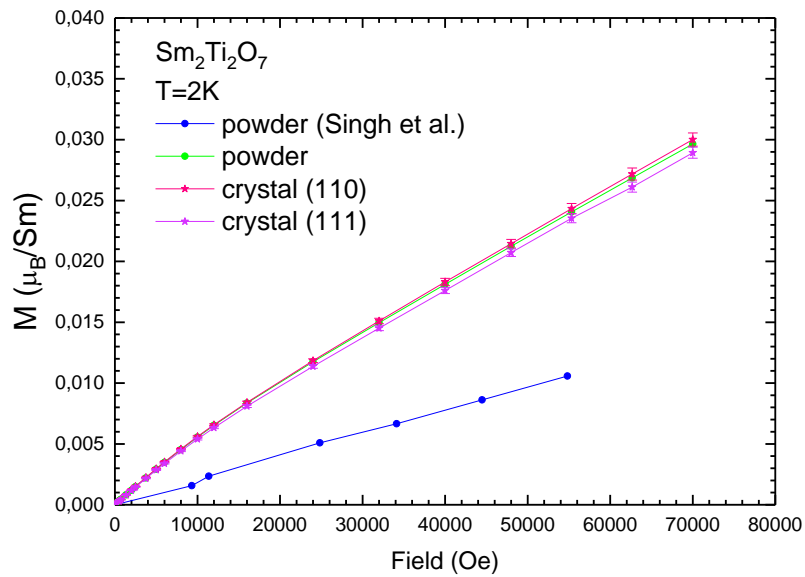


Fig.31: Magnetization in function of field, at temperature $T=2\text{K}$, in comparison with experimental data found in [11].

Finally, saturation is not reached until 7T by any of our samples nor in the reference, which prevents us from comparing it with the expected value for $J=5/2$ referent to the ion of Sm^{3+} .

7.3 Specific Heat data

The first aspect we notice in the specific heat data (fig.32) is a pronounced λ -like peak at 0.35K, which possibly indicates a phase transition, exactly as reported in [11]. Here, specific heat is measured for the single crystal sample under zero field, on the

temperature range of 500mK-100K. The first step to start the specific heat analysis is to isolate the magnetic contribution, which can be done via the subtraction of T^3 contribution at low temperatures (which is the Debye contribution of phonons, as we have seen in (32) or the subtraction of data of a similar non-magnetic structure with the same crystal structure. In this work, we have opted for the second alternative since the antiferromagnetic contribution to the specific heat is also T^3 ; We measured specific heat data for the compound $\text{Lu}_2\text{Ti}_2\text{O}_7$, where Lu^{3+} is an appropriate non-magnetic option of lanthanide since it stays close to Samarium in the periodic table (and therefore we can expect a similar structure), besides presenting a pyrochlore structure. This sample was prepared by the sol-gel method by prof. Flávio Vichi (IQ-USP), resulting in a white powder sample. However, we can see in fig.33-a) that the data does not fit perfectly, which is expected to a certain amount since the structures are not exactly the same. To fix this disparity, we have divided the non-magnetic data by a factor of 1.9, which resulted in a good convergence with the magnetic data along the range of $T=6\text{K}$ and 10K .

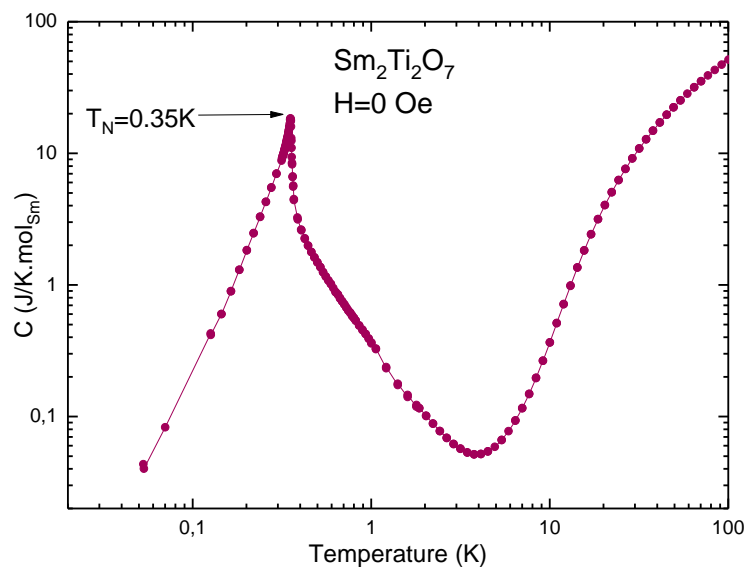
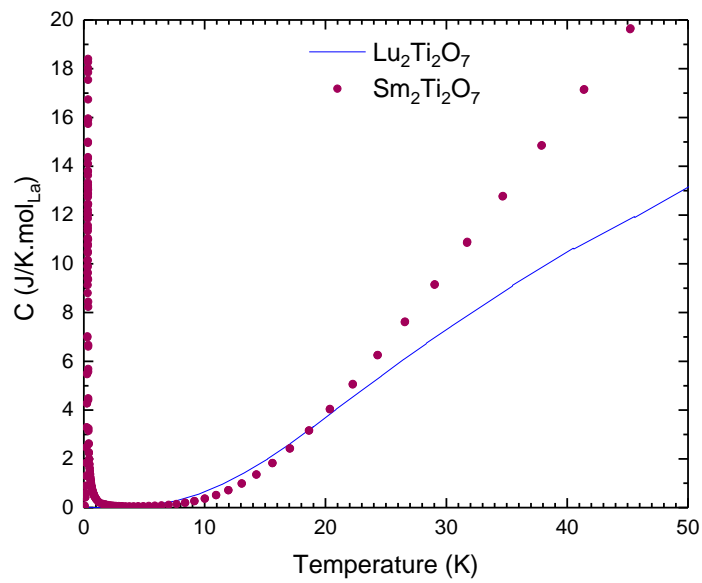


Fig. 32: Specific Heat data of a single crystal sample of $\text{Sm}_2\text{Ti}_2\text{O}_7$ measured at zero field and oriented in a random direction. The curve is a guide to the eye.

a)



b)

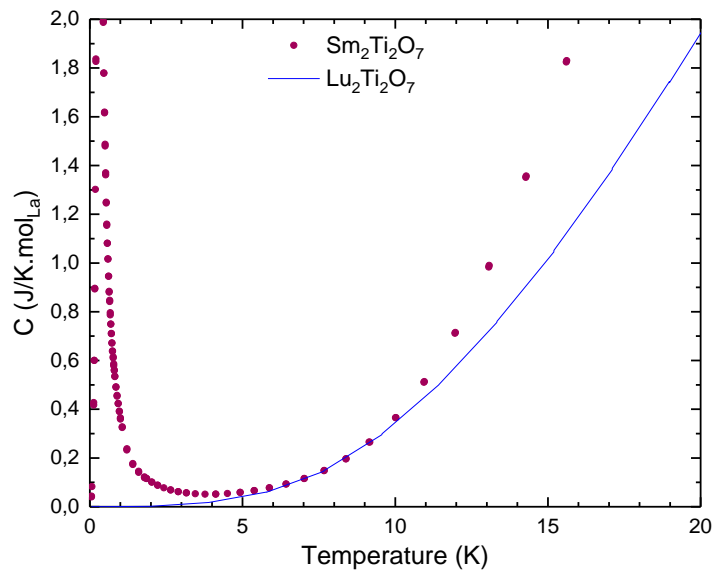


Fig. 33: Subtraction of lattice contribution at low temperatures, at $H=0\text{T}$, for a single crystal sample of $\text{Sm}_2\text{Ti}_2\text{O}_7$ oriented at a random direction; Specific Heat normalized by mol of Lanthanide (either Sm or Lu). In **a)**, we see the raw data of specific heat for both compounds $\text{Sm}_2\text{Ti}_2\text{O}_7$ and $\text{Lu}_2\text{Ti}_2\text{O}_7$ and in **b)**, the non-magnetic data after dividing it by an arbitrary factor of 1.9 to approximate it to the magnetic data of $\text{Sm}_2\text{Ti}_2\text{O}_7$.

One way of analyzing the phase transition is to draw a phase diagram with the peak values of the specific heat in function of the applied field. We have repeated this

procedure to both single crystal and polycrystalline samples, which enabled us to identify both antiferromagnetic behavior and absence of anisotropy (fig.34 a) and b), respectively).

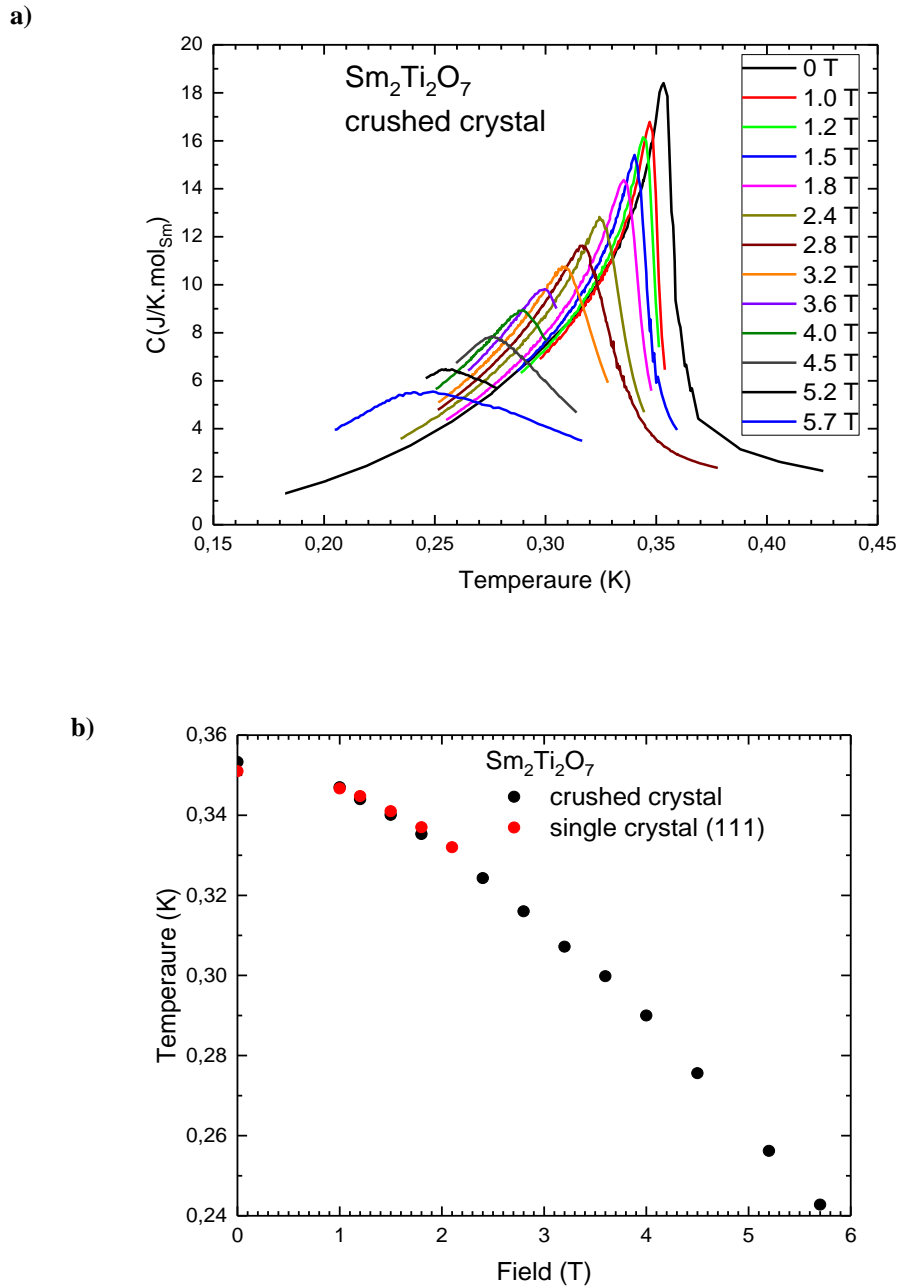


Fig.34: a) Specific heat data under several values of applied field, for crushed crystal (polycrystalline) sample near transition range and **b)** phase diagram for both polycrystalline and single crystal (oriented in direction (111)) samples.

To ratify the antiferromagnetic behavior that takes place until the phase transition, we have fit a linear function in T^3 around low temperature ($T < 0.34\text{K}$), where the energy of the system should be too low to disarrange the spins, as expected for the antiferromagnetic magnons. We notice that the fitting worked well in the same range employed by Mauws et al. (Fig. 35) [13]

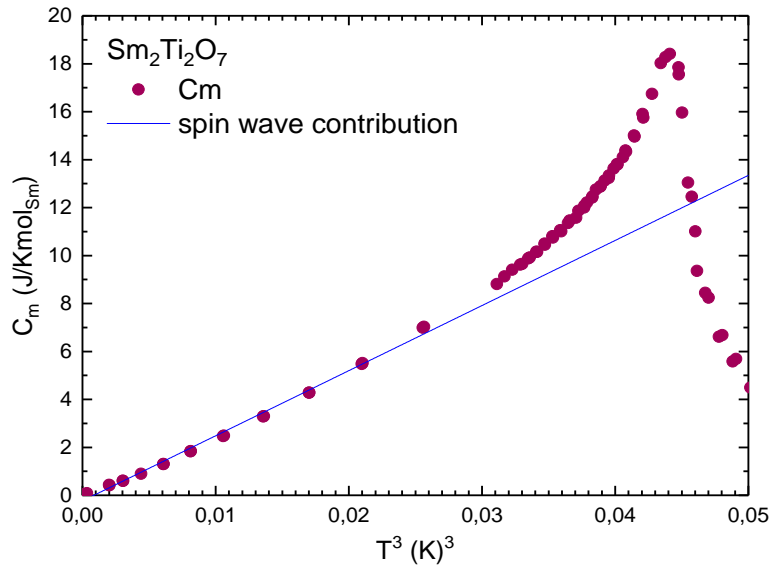


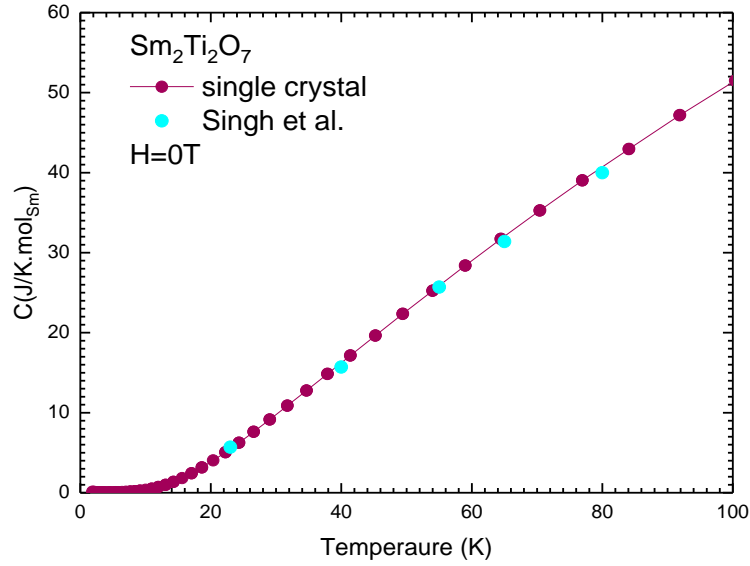
Fig. 35: Linear fitting in the heat capacity data for a single crystal sample of $\text{Sm}_2\text{Ti}_2\text{O}_7$ oriented at a random direction, in T^3 , at low temperatures ($T < 0.34\text{K}$) and zero field, which corresponds to the magnon contribution of an Antiferromagnetic system.

Using the intercept value derived from the spin wave contribution fitting and the lattice parameter $a = 10.227\text{\AA}$ [11], we can use the equation 51 to derive magnon velocity $v_{\text{mag}} \approx 192\text{m/s}$.

As a comparative, we have contrasted our specific heat data with the ones in Singh et al. [11] and Mauws et al. [13], our two reference papers for this compound. We can notice how our specific heat data is in good agreement with the presented in both works, at low and higher temperatures, as we can observe in comparison with the data in ref.[13], in fig.36-b); Notice that the difference between the intensities found in our data and in the reference can derive from the technique employed for measurement,

which may result in a better resolution of the peak (as we see in the Slope Analysis technique). The temperature found for the transition is the same of 0.35K.

a)



b)

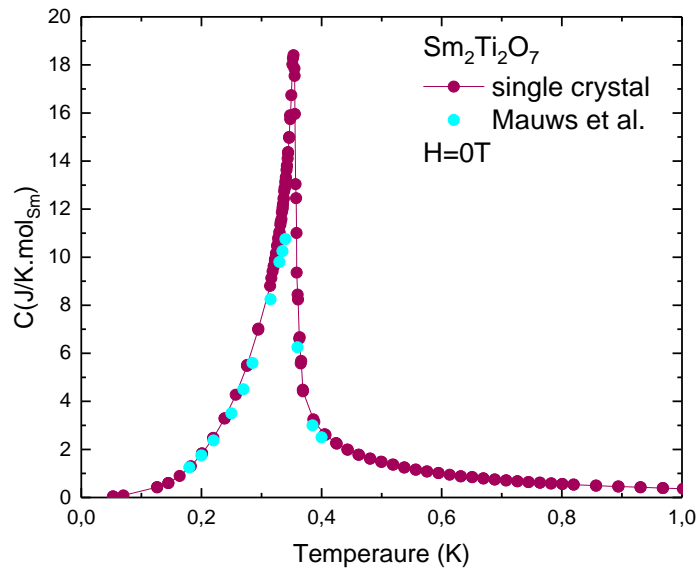


Fig.36: Comparison between the data acquired in this work (dark pink) and the data from the reference papers (cyan), both single crystal samples [13][11].

Finally, in conclusion of the specific heat analysis, we integrated the magnetic specific heat data between $T=0.05\text{K}$ and $T=6\text{K}$ to obtain the variation of entropy of the system. We notice that the saturation value surpasses a little the expected value for the

spin 1/2, $R \ln 2$, giving us 102% of this value; While integrating over a reduced interval of 0-1K, as done in ref.[11], we get a saturation that corresponds to 98% of the same value. There is a noticeable difference between the values presented at the references, which were respectively 87% [11] and 84% [13] and one point to be stressed is that the authors opted to subtract the lattice of a different compound ($\text{La}_2\text{Ti}_2\text{O}_7$), which may explain the difference between the shown results (fig.37).

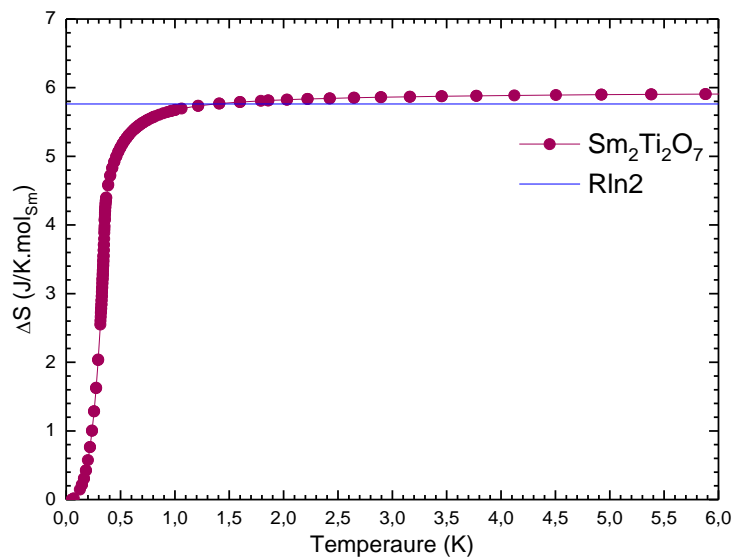


Fig.37: Variation of entropy for a single crystal sample of $\text{Sm}_2\text{Ti}_2\text{O}_7$ in comparison with the expected value of $R \ln 2$ expected for a Ising spin system. Results derived from the integration of magnetic specific heat data between the interval 0.05-6K.

Chapter 8

Results and Discussion: Nd₂Ti₂O₇

The major interest in studying such structure as Nd₂Ti₂O₇ lays on the fact that monoclinic structures of rare-earth titanates have been reported for not presenting magnetic frustration at low temperatures and therefore presenting magnetic ordering. On the other hand, this sample is also characterized by the competition between crystal field and exchange interactions, which may result in complex behavior specially close to the ordering. [12] These features may start to explain the motives behind the low exploitation of this sample, in a similar way as we have witnessed for the sample of Sm₂Ti₂O₇.

For the structure Nd₂Ti₂O₇ (space group P2₁), we worked both with a single crystal sample and a polycrystalline sample, the first grown by the FZ method and the second, derived by the sol-gel method. We analysed the X-Ray data of the polycrystalline sample to confirm the absence of impurities and the Laue backscattering method to find previously chosen directions of the single crystal sample. We were able to make measurements of heat capacity and magnetization at very low temperatures, which allowed us to see a transition peak that haven't been observed in the literature until the moment. The magnetization measurements were carried out on a Quantum Design SQUID and a VSM while the heat capacity measurements were obtained through Quantum Design's PPMS, sometimes with a coupled refrigerator.

8.1 Preliminary Analysis

We started our studies of the single crystal sample looking for the directions (100), (010) and (001), which were adopted to analyse in the reference [12]. We used the Laue backscattering method and the software Clip to find these directions, as we may see in the fig.38 and fig.39 below.

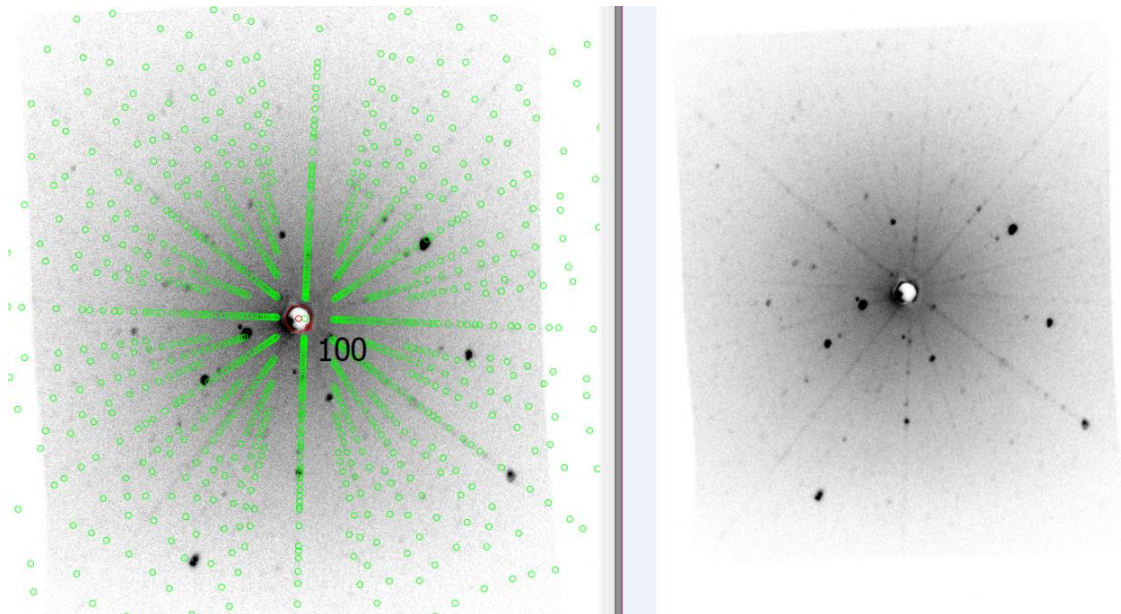


Fig.38: diffraction pattern found for the direction (100) of the single crystal sample of $\text{Nd}_2\text{Ti}_2\text{O}_7$; On the left, we see the theoretical dots for the direction (100) given by the software Clip and on the right, the image derived from the Laue backscattering.

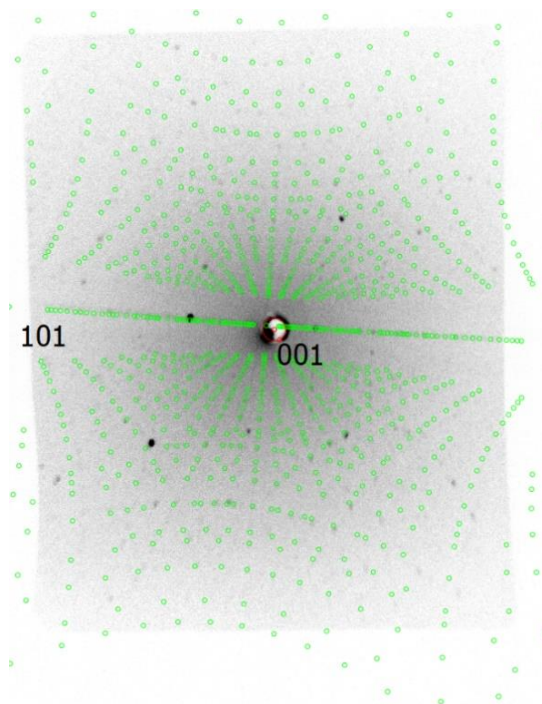


Fig.39: diffraction pattern for the direction (001) of the single crystal sample of $\text{Nd}_2\text{Ti}_2\text{O}_7$, given by the software Clip.

Observing comparatively the diffraction pattern for both directions (100) and (001), we may notice how much they differ, instead of what we've seen in the case of $\text{Sm}_2\text{Ti}_2\text{O}_7$. This is the first indication of low symmetry for this sample, which is already expected for a monoclinic configuration.

In possession of a polycrystalline sample, we performed the analysis of its X-Ray data to check its purity. We used, again in a similar way done for the $\text{Sm}_2\text{Ti}_2\text{O}_7$ crushed sample, data in ref. [25] to compare the localization of the peaks (fig. 40).

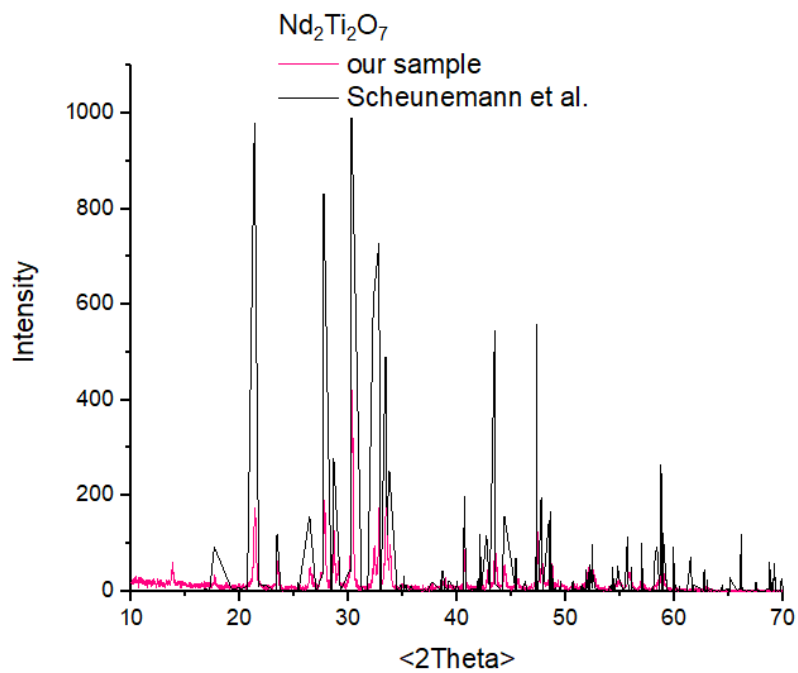


Fig. 40: X-ray diffraction data from our sample of powder originated from sol-gel synthesis (pink) and the data found in ref [25] for a single crystal sample of $\text{Nd}_2\text{Ti}_2\text{O}_7$.

We can observe that the data doesn't seem to be exactly compatible, which may indicate structural damage of the sample, such as oxygen vacancies. To a better understanding of the incompatibility of some of the peaks, it's necessary to apply a refinement technique on the X-Ray data.

8.2 Magnetic Measurements

We started our magnetization analysis of the samples of $\text{Nd}_2\text{Ti}_2\text{O}_7$ by the Curie-Weiss analysis (fig. 41); We applied a linear fitting in the range of 50K-300K except for the sample in direction (100), for which the fitting was better after 100K. We notice that the lines have similar inclinations except for the polycrystalline sample, for which the linear fitting is clearly not a good option.

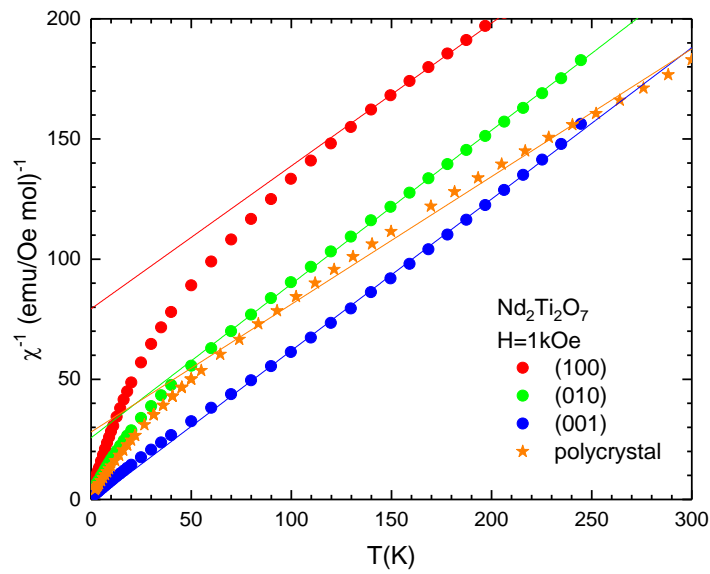


Fig.41: Inverse of susceptibility for the polycrystalline and single crystal in directions (100), (010) and (001) for the $\text{Nd}_2\text{Ti}_2\text{O}_7$ sample.

	our sample		Xing et al. [12]	
	μ_{eff}	θ	μ_{eff}	θ
powder	$3.89 \mu_B$	- 240K	$3.49 \mu_B$	- 42.1K
(100)	$3.68 \mu_B$	- 250K	$3.45 \mu_B$	- 128.9K
(010)	$3.55 \mu_B$	- 160K	-	-
(001)	$3.57 \mu_B$	- 120K	$3.44 \mu_B$	10.4K

Table 3: parameters derived from Curie-Weiss fitting of data in all three directions of single crystal and powder in comparison with the data found by Xing et al. for both directions (100) and (001) and powder samples in ref. [12].

It is worth noticing that in the ref. [12], the analysis for powder was done over a single crystal crushed while we had a polycrystalline sample prepared by sol-gel method. Looking for the table 3, we see how the values for μ_{eff} are compatible with each other and with the values derived in the reference; In addition to that, the values we derived from our samples are closer to the theoretical value of $3.62 \mu_{\text{B}}$ for a free Nd ion. On the other hand, the values derived for Curie-Weiss temperature are not compatible with the ones presented in the reference; We see that the parameter values derived for the polycrystalline sample and for the crystal in direction (100) are the worst, in good agreement with the fact that their fitting are seemingly worse than the others. These values reaffirm still the antiferromagnetic behaviour of the sample.

Advancing with the magnetic analysis, we have measured the magnetization in function of the external field for the three directions of the single crystal and for the powder sample (fig. 42). Here it's clear the highly anisotropic aspect of the sample, which is expected for a very antisymmetric lattice as the monoclinic configuration. On the other hand, looking for the data presented in ref. 12, we may see the saturation point for the directions (100), (001) and for the polycrystalline sample at $T=2\text{K}$ occurs around the values 0.8, 1.9 and $1.6 \mu_{\text{B}}/\text{Nd}$, which are very compatible with the data derived in this work, except for the powder sample – which, as we've discussed before, can have structural deficiencies, besides being synthesized by a different method as observed in the reference. We may notice also that the saturation point presented by measurements along (001) are more than twice as much as the ones presented by directions (100) and (010), which indicates (001) as the easy axis of spins in Nd^{3+} , as pointed in [12]. An analogue behaviour was observed on the susceptibility data.

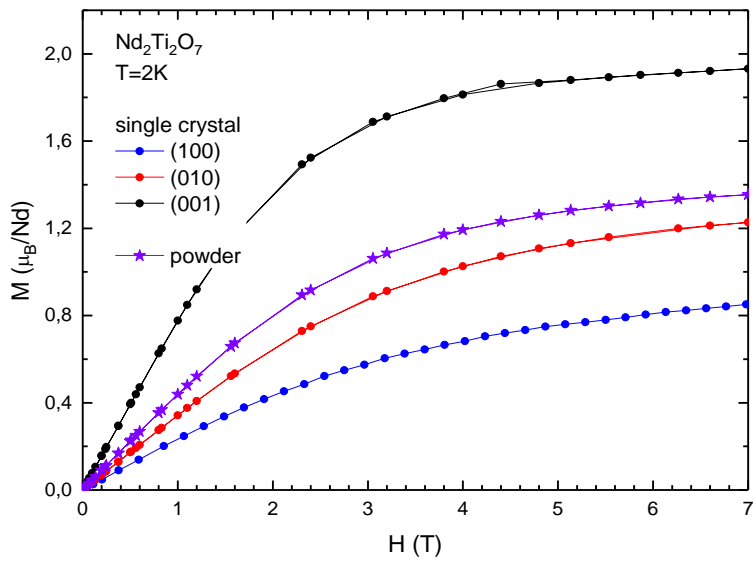


Fig. 42: Magnetization in function of field for three crystallographic directions and powder sample, for T=2K.

Finally, we measured the ac susceptibility until low temperatures around 500mK, which allowed us to see the transition peak around the temperature of 650mK – information which has not been observed yet in any previous work (fig.43). We can compare the transition temperature derived here with the one derived in the following section of specific heat analysis to see if they are compatible.

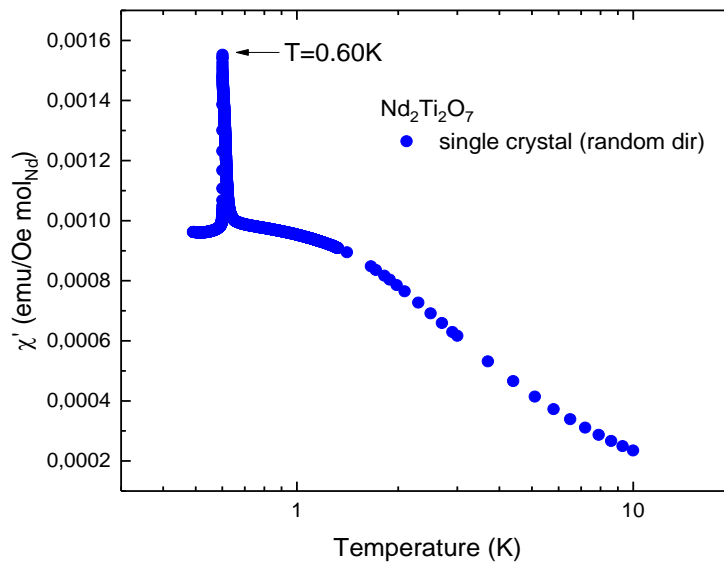


Fig.43: Susceptibility in function of temperature. A pronounced transition peak is observed at $T=600\text{mK}$.

Through the Weiss temperature and the transition temperature, we derive the frustration index that revolves between 200 and 416, which is more than two orders of magnitude greater than the value found for $\text{Sm}_2\text{Ti}_2\text{O}_7$ and only confirms the highly frustration that characterizes this system.

8.3 Specific Heat data

The first aspect we notice in the specific is the pronounced λ -like peak at temperature 0.62K, in a similar fashion as observed in the sample of $\text{Sm}_2\text{Ti}_2\text{O}_7$ (fig. 44). We cannot compare this information with the data presented in previous papers since there hasn't been reports at this range of temperature but we can see through the comparison with the transition temperature observed in the ac susceptibility data that they are compatible. We can also notice how this transition temperature is the same for both single crystal and polycrystalline samples, as expected, although the intensity of specific heat is much larger in the single crystal sample, probably because of a better

thermal contact between sample and platform or once again because of the technique employed for data acquisition.

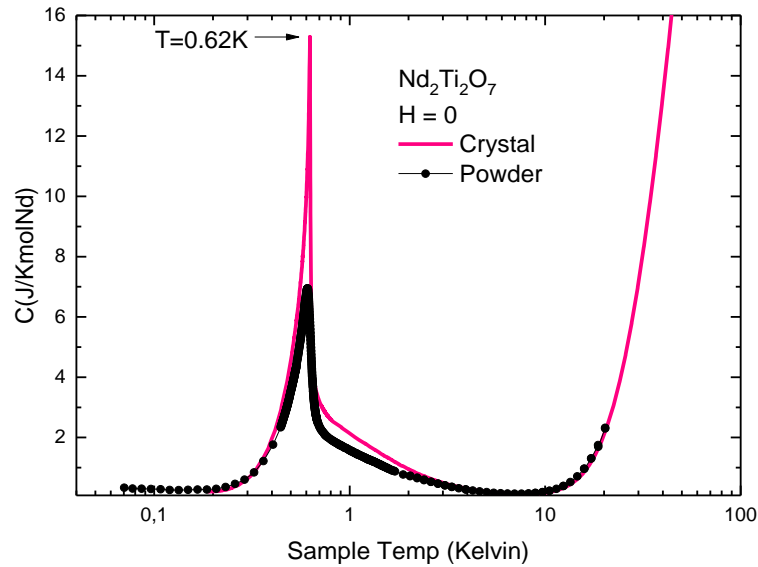


Fig. 44: Heat capacity of single crystal and polycrystalline sample, with transition temperature at 0.62K, for zero field.

While studying the heat capacity behaviour under several values of external field we notice that, as the field is increased, the transition peak disappears as another less pronounced broad maximum appears. This maximum moves to the right with the applied field and becomes smoother, reassembling the Schottky anomaly behaviour. While trying to apply the simplest model of two-level energy given in (53), we notice the fitting is not good, in contrast with the data presented in [12], whose behaviour is clearly different and the peaks are more pronounced and well-defined (fig.45). The fitting is better only for the lower field 1.8T, for both samples. It is worth mentioning that the authors in [12] do the lattice contribution subtraction through the $\text{La}_2\text{Ti}_2\text{O}_7$ data subtraction. Since we don't have this sample and $\text{Lu}_2\text{Ti}_2\text{O}_7$ has a different structure from $\text{Nd}_2\text{Ti}_2\text{O}_7$, we were only able to do this subtraction through the T^3 analysis.

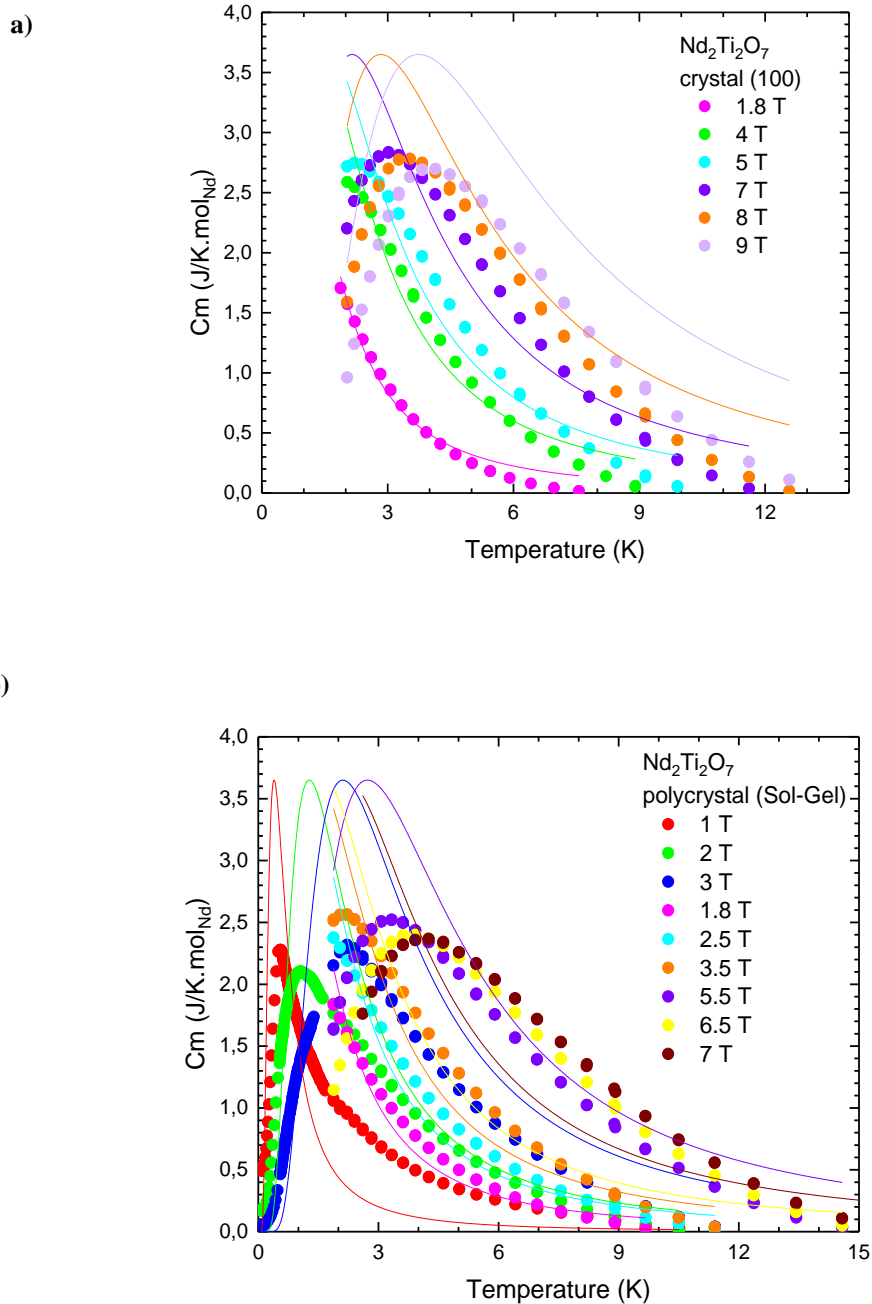


Fig.45: Schottky anomaly analysis applied to heat capacity data in function of temperature, for several values of field, for the polycrystalline sample.

We can observe in fig. 46 how the subtraction of the lattice contribution reduces the heat capacity; analyzing the data presented by [12], we notice how the peak in the heat capacity data coincides with Schottky analysis. In other words, the lattice subtraction applied didn't affected the intensity of the data presented by the authors, which may lead

us to believe that the subtraction wasn't correct. It is important to notice that the use of non-magnetic isomorph compounds may not be the right choice to subtract out the lattice contribution since the impact of stretching and bending force constants can vary greatly depending on the ion in the structure. [26] Observing the fitting in T^3 , we see how well it adjusts at higher temperatures, as expected for the Debye's model.

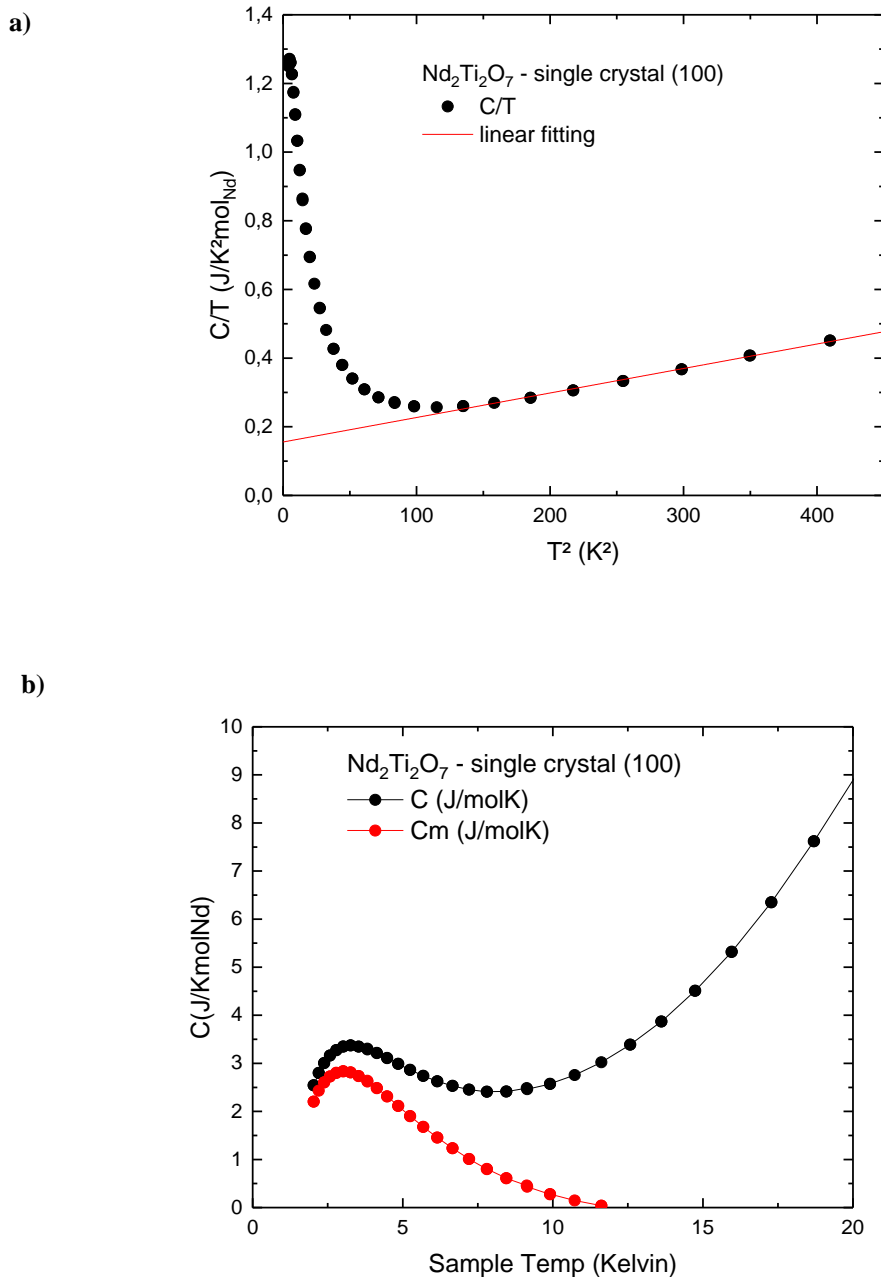
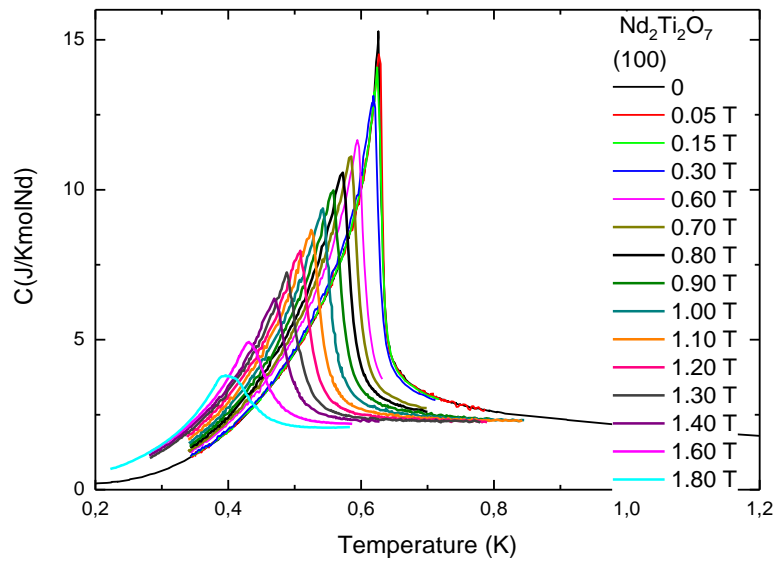


Fig.46: a) Lattice subtraction following the dependence in T^3 b) Heat Capacity for a single crystal sample in direction (100) before and after lattice subtraction. The measurement was taken at $H=0T$.

Once again, we analyze the phase transition drawing the phase diagram with the peak values of the specific heat in function of the applied field (fig.47-b)). This enabled us to identify antiferromagnetic behavior. We couldn't do measurements along other directions of the single crystal sample and polycrystalline sample to verify anisotropy.

a)



b)

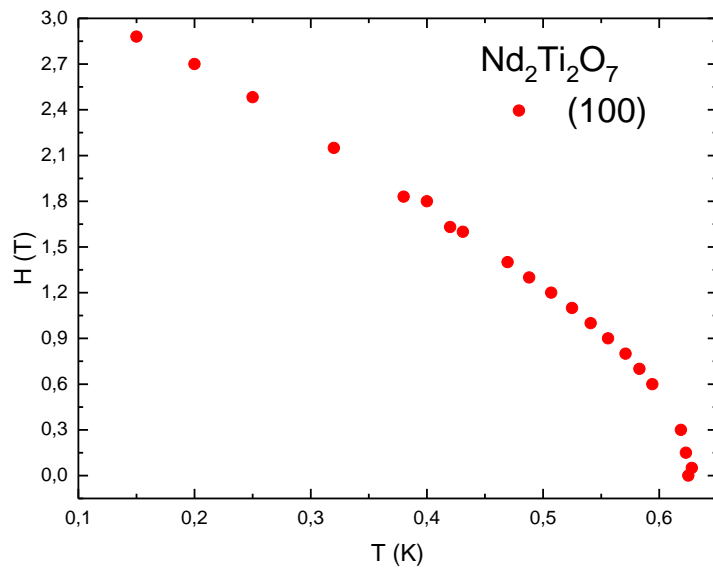


Fig.47: a) Specific heat data under several values of applied field, for crushed crystal (polycrystalline) sample near transition range and **b)** phase diagram for single crystal (oriented in direction (100)).

Finally, we have plotted the specific heat data for lower fields (left) and higher fields (right) to see how the maximum behaves – in the first case, it goes to lower temperatures until it almost vanishes, indicating a phase transition, and in the second case, it moves to higher temperatures and becomes broader, indicating a typical behavior of Schottky anomaly (fig. 48).

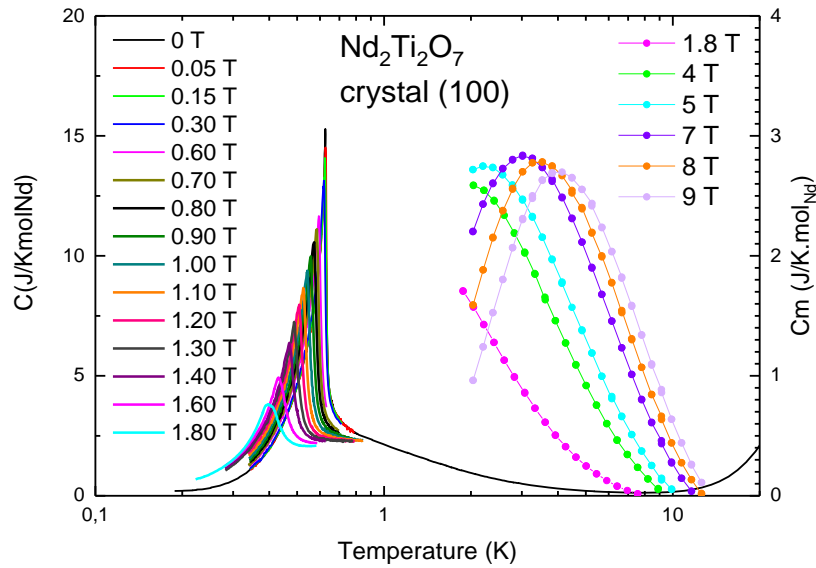


Fig.48: Specific heat at low fields (left) and higher fields (right).

We then fitted a polynomial function in T^3 at low temperatures ($T < 0.6\text{K}$) in the magnetic data, as expected for antiferromagnetic magnons (fig. 49). As we can see in the fitting below, the model works well for both single crystal sample and polycrystalline sample.

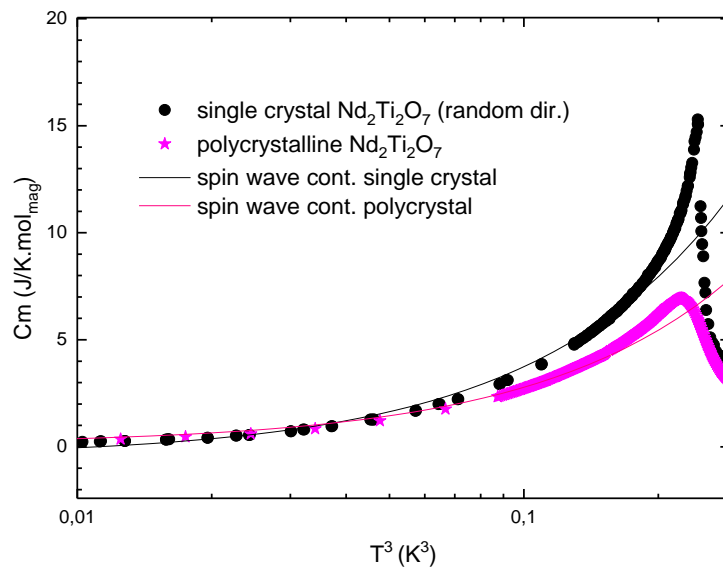


Fig. 49: Linear fitting in the heat capacity data, in T^3 , at low temperatures ($T < 0.34\text{K}$), which corresponds to the magnon contribution of an Antiferromagnetic system. The measurements were taken at $H=0\text{T}$.

Finally we integrated the magnetic specific heat data between $T=0.19\text{K}$ and $T=10\text{K}$ to obtain the variation of entropy of the system (fig. 50). We notice that the saturation value of the single crystal sample surpasses a little the expected value for the Ising spin, $R\ln 2$, giving us 104% of this value while integrating the polycrystalline sample gives us 83% of the same expected value. The authors in the reference weren't able to study heat capacity at a good enough interval to derive the variation of entropy so we don't have another data to compare it with; On the other hand, the behavior of both single crystal and polycrystalline samples are similar and the difference observed is clearly a result of the difference previously observed in the intensity of transition peaks in heat capacity.

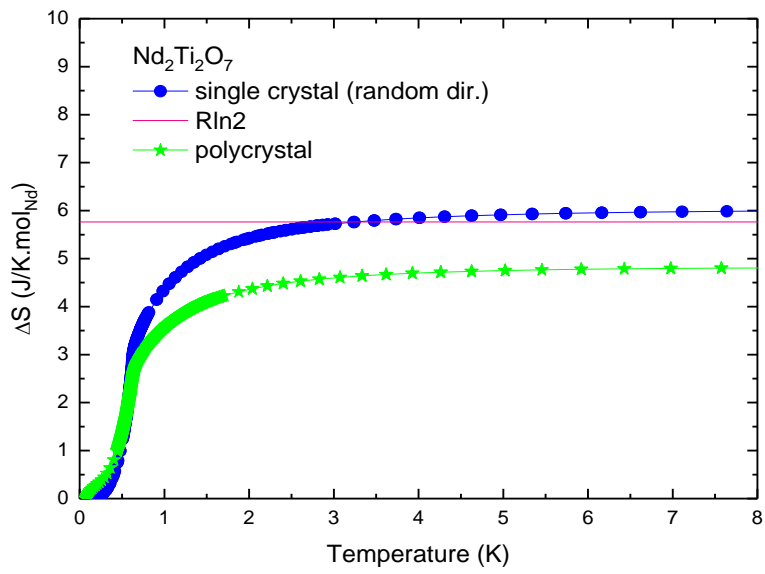


Fig.50: Variation of entropy of single crystal and polycrystalline samples of $\text{Nd}_2\text{Ti}_2\text{O}_7$ in comparison with the expected value of entropy for a Ising spin system. Results derived from the integration of magnetic specific heat data between the interval 0.19-10K.

Chapter 9

Conclusion

In this work, we have studied a single crystal sample of $\text{Sm}_2\text{Ti}_2\text{O}_7$ and both single crystal and polycrystalline samples of $\text{Nd}_2\text{Ti}_2\text{O}_7$. The single crystal samples were obtained through the FZ method while the polycrystalline sample was obtained by the Sol-gel method. A polycrystalline sample of $\text{Sm}_2\text{Ti}_2\text{O}_7$ was produced by crushing a piece of the single crystal sample above mentioned.

We have selected and found directions for our single crystal samples through the Laue backscattering method and we have compared the X-Ray diffraction data from our samples with the ones found in articles to verify the presence of impurities in our samples, which is a good first analysis.

In the sample of $\text{Sm}_2\text{Ti}_2\text{O}_7$, we have observed a broad maximum around $T=128\text{K}$, close enough to the behavior reported on the reference, which is attributed to the crystal field around Sm^{3+} . We have also fitted a modified Curie-Weiss model and observed the compatibility of the derived parameters: they reassert the singularity of ion Sm^{3+} with its reduced value of μ_{eff} and the antiferromagnetic behavior. We also observe the presence of anisotropy at higher temperatures, which does not occur at $T=2\text{K}$, where the measurement of $M \times H$ only shows the compatibility between the data for the three directions studied and the absence of saturation until 7T . We can also observe an incompatibility with the data presented in the reference. In the heat capacity data, we were able to notice a lambda-like pronounced peak at $T=0.35\text{K}$, exactly as reported in the reference, indicating a phase transition. We have also derived a phase transition diagram which indicates the absence of anisotropy and confirms the antiferromagnetic behavior. Finally, we have integrated the specific heat data to derive the variation of entropy, which surpasses a little the expected value for Ising spins $R \ln 2$, indicating that maybe we have overestimated the heat capacity data integrated.

Now, concerning the sample of $\text{Nd}_2\text{Ti}_2\text{O}_7$, we have noticed the strong anisotropy of the sample already in the difference of diffraction patterns between the different directions. Analyzing the magnetic data, we see through the Curie-Weiss fitting that the values of μ_{eff} are similar and even compatible with the ones derived in the reference and the theoretical value of $3.62 \mu_B$; On the other hand, the values of θ change a lot with the orientation of the sample and are not compatible with the ones seen in the reference but they confirm the antiferromagnetic behavior. Analyzing the magnetization as a function of external field, we see the strong anisotropy and the preference of spins to align along the (001) direction. The saturation point varies with the direction but they are all compatible with the values observed in the reference. Finally, we have observed a pronounced peak around $T=0.60\text{K}$, which indicates a transition point that was never observed before. We have also noticed that the Schottky anomaly model doesn't fit well in our data presenting a visible difference in the magnitude of the peaks, au contraire to what we observe in the reference data. On the other hand, the lattice subtraction clearly doesn't affect the magnitude of the peak in the magnetic heat capacity data presented in the reference, which indicates that the method applied to lattice subtraction isn't a good one.

In a future work, it's necessary to employ a refinement (such as the Rietveld technique) on the X-Ray data in order to identify the possible defects on the structures of the samples. It's also important to do a neutron diffraction analysis to confirm the analysis made in this work.

Chapter 10

References

-
- 1 C. Kittel. Introduction to Solid State Physics. John Wiley & Sons (2005)
 - 2 R.L. Carlin. Magnetochemistry. Springer (1986).
 - 3 J.E.Greedan. J. of Alloys and Compounds 408-412 (2006) 444-455.
 - 4 J.T.Chalker. Geometrically frustrated antiferromagnets: statistical mechanics and dynamics. Lecture notes for Trieste Summer School (Aug 2007).
 - 5 W.Witczak-Krempa, G.Chen, Y.B.Kim, L. Balents. Ann Rev. Cond. Mat. Phys. **5** 57 (2014).
 - 6 chemicalstructure.net
 - 7 C.R.Wiebe, A.M.Hallas. APL Mater. 3, 041519 (2015).
 - 8 E.S.R.Gopal. Specific Heats at low Temperatures. Plenum Press (1966).
 - 9 N.W. Ashcroft and N.D. Mermin. Solid State Physics. Harcourt College Publishers (1976).
 - 10 N.Ishizawa, K.Ninomiya, T.Sakakura, J.Wang Acta Cryst. **E69** i19 (2013).
 - 11 S.Singh, S.Saha, S.K.Dhar, R.Suryanarayanan, A.K.Sood, A.Revcolevschi. Phys.Rev.B **77**, 054408 (2008).
 - 12 H.Xing, G.Long, H.Guo, Y.Zou, C.Feng, G.Cao, H.Zeng, Z.-A.Xu. J.Phys.Cond.Matter 23 216005 (2011).
 - 13 C.Mauws, A.M. Hallas, G. Sala, A.A. Aczel, P.M. Sarte, J. Gaudet, D. Ziat, J.A. Quilliam, J.A. Lussier, M. Bieringer, H.D. Zhai, A. Wildes, M.B. Stone, D. Abernathy, G.M. Luke, B.D. Gaulin, C.R. Wiebe. Phys. Rev. B **98**, 100401 (R) (2018).
 - 14 Z.M.Sao, S.Sartzek, A.Ferri, M.Rguiti, L.Dupont, P.Roussel, R.Desfeux. J.Mater.Chem. **22** 9806 (2012).
 - 15 G.Balakrishnan, O.A.Petrenko, M.R.Lees, D.McK Paul. J.Phys.: Condens. Matter **10** L723 (1998)
 - 16 B.D.Cullity. X-Ray Diffraction. Addison-Wesley Publishing Company (1956).
 - 17 QUANTUM DESIGN. The Magnetic Property Measurement System – MPMS MultiVuApplication User’s Manual. 3.ed. San Diego, USA (2004).

18 Magnetic Property Measurement System, SQUID VSM User's Manual. Quantum Design, 17th edition, San Diego (2009).

19 S. Foner. Versatile and sensitive vibrating-sample magnetometer. *The Review of Scientific Instruments* **30, 7**, 548-557 (1959).

20 M. Nikolo. Superconductivity: A guide to alternating current susceptibility measurements and alternating current susceptometer design. *American Journal of Physics* **63, 57**, 57-65 (1995).

21 Physical Property Measurement System, Heat Capacity Option User's Manual. Quantum Design, 17th edition, San Diego (2010).

22 I.S.Oliveira, V.L.B. de Jesus. *Introdução à Física do Estado Sólido*. Livraria da Física. São Paulo (2005).

23 F. Pobell. *Matter and Methods at Low Temperature*. Springer, New York (1966).

24 O.Knop, F.Brisse, L.Castelliz. *Can. J. Chem.* 47 971 (1969).

25 K. Scheunemann, H. Mueller Buschbaum. *Journal of Inorganic and Nuclear Chemistry* 37 2261 (1975).

26 S.Nandi, Y.M.Jana, H.C.Gupta. *J. of Physics and Chemistry of Solids* **115** 347-354 (2018).